

# Advances in Monitoring Black Sea Dynamics: A New Multidecadal High-Resolution Reanalysis

Leonardo Lima<sup>1</sup>, Diana Azevedo<sup>1</sup>, Mehmet Ilicak<sup>2,1</sup>, Eric Jansen<sup>1</sup>, Filipe Costa<sup>1</sup>, Adil Sozer<sup>1,3</sup>, Pietro Miraglio<sup>1</sup>, Emanuela Clementi<sup>1</sup>

<sup>1</sup>CMCC Foundation – Euro-Mediterranean Center on Climate Change, Italy

<sup>2</sup>Eurasia Institute of Earth Sciences, Istanbul Technical University, Istanbul, Turkey

<sup>3</sup>Ordu University, Fatsa Faculty of Marine Science, Ordu, Turkey

*Correspondence to:* Leonardo Lima (leonardo.lima@cmcc.it)

**Abstract.** The Black Sea regional reanalysis serves as an essential tool for understanding the Black Sea’s response to climate variability and advancing regional ocean monitoring efforts. In particular, the Black Sea reanalysis (BLK-REA) is built with high spatial resolution,  $1/40^\circ$  horizontal grid and incorporating 121 vertical levels. The model implementation includes lateral open boundary conditions (LOBC) at the Marmara Sea, allowing more accurate inflow/outflow dynamics through the Bosphorus Strait. BLK-REA assimilates sea level anomaly (SLA) and in-situ observations and applies a heat flux correction via sea surface temperature relaxation. The data assimilation system uses a background error covariance matrix evaluated through monthly EOFs over decadal periods to capture seasonal and decadal variability, and an observation-based mean dynamic topography is used for SLA assimilation. When compared to available observations, the numerical results show high accuracy, with the largest temperature errors observed in the upper layers, primarily linked to the formation of the seasonal thermocline during the summer months. The SLA anomaly error is consistently around 0.02 m from the year 2000 onwards, and regions with elevated SLA errors are closely associated with the Rim Current and its mesoscale variability. Furthermore, BLK-REA plays a crucial role in generating Ocean Monitoring Indicators, which are essential for tracking and assessing the impacts of climate change in the Black Sea. For example, temperature data indicate ongoing warming in the 25 to 150 m layer, where the Cold Intermediate Layer is located. The system is regularly updated, with the next version expected to improve both the model and DA components. For a future perspective, the next BLK-REA will expand the domain to include the Azov Sea and will feature an enhanced Bosphorus LOBC.

## 1 Introduction

The Black Sea is a semi-enclosed basin linked to the Marmara Sea through the Bosphorus Strait, the narrowest part of the Turkish Strait System (TSS). The TSS continues through the Dardanelles Strait, which connects the Marmara Sea to the Mediterranean. Salty waters originating from the Mediterranean Sea flow into the Black Sea through the TSS, serving as its main source of salinity. Despite this influx of saltier waters, the Black Sea is mainly considered a freshwater basin,

31 characterized by a negative balance between evaporation ( $E$ ), precipitation ( $P$ ), and runoff ( $R$ ):  $E - P - R$ . This imbalance  
32 is compensated by a two-layer exchange through the Bosphorus Strait, where a stronger flow of the fresher upper layer moves  
33 southward toward the Marmara Sea (Beşiktepe et al., 1994; Altiok and Kayışoğlu, 2015). The surface circulation in the Black  
34 Sea is primarily driven by the Rim Current, a semi-permanent cyclonic (counterclockwise) jet that flows along the edges of  
35 the basin. Along its path, this current interacts with multiple cyclonic gyres within its core and anticyclonic (clockwise) eddies  
36 along its peripheries, such as the Batumi and Sevastopol eddies (Oguz et al., 1993; Korotaev et al., 2003).

37 An important feature of the Black Sea is the Cold Intermediate Layer (CIL), a cold water mass generated each winter through  
38 surface cooling and convective mixing. The CIL helps the ventilation of the sub-surface of the Black Sea (Özsoy and Ünlüata,  
39 1997) and is typically defined by water temperatures below  $8^{\circ}\text{C}$  and extends between depths of 30 m to 80 m (Ivanov et al.,  
40 2001). The formation of the CIL in the Black Sea is primarily driven by convective processes during cold winters, where cool  
41 surface waters become denser and sink to intermediate depths. Recent studies have emphasized that CIL variability is not  
42 solely controlled by local winter conditions but is the result of a complex interplay between atmospheric forcing, lateral  
43 advection, and oceanic circulation (Korotaev et al., 2014; Miladinova et al., 2018; Capet et al., 2020). For example, the Rim  
44 Current and associated mesoscale eddies create localized upwelling and downwelling regions, influencing the CIL distribution  
45 (Podymov et al., 2023).

46 Understanding the circulation and physical processes of the Black Sea from the past to recent years can be supported by ocean  
47 reanalyses. These products use state-of-the-art models driven by atmospheric forcing and data assimilation, which integrates  
48 high-quality multi-year satellite and in situ datasets to reconstruct historical ocean conditions (Haines et al., 2018; Yang et al.,  
49 2025). They are crucial for monitoring, as they provide insight into the ocean's evolution in response to external forcing, and  
50 they allow for the assessment of how environmental changes may affect marine biota, ecosystems, and activities dependent on  
51 the health of marine environments.

52 This work presents a new high-resolution Black Sea reanalysis (hereafter referred to as BLK-REA), developed within the  
53 Copernicus Marine Service, which updates the model components and the variational data assimilation system, assimilating  
54 both in situ and satellite observations to provide a consistent reconstruction of the Black Sea's physical state. BLK-REA  
55 incorporates improved lateral open boundary conditions to better represent exchange flows through the Bosphorus Strait, an  
56 improved freshwater budget, and a high-resolution model configuration that allows better representation of mesoscale and  
57 submesoscale processes. Assimilation of satellite and in situ datasets ensures that the reconstructed historical ocean state is  
58 physically consistent and captures the evolution of key monitoring indicators for the Black Sea. Previous Black Sea reanalyses,  
59 also developed within the framework of the Copernicus Marine Service, have served as valuable tools for improving our  
60 understanding of the Black Sea's response to climate change. For example, they revealed a recent warming of the Black Sea's  
61 surface, observed in both sea surface temperature (SST) and subsurface temperature (Mulet et al., 2018; Lima et al., 2021).  
62 An ocean monitoring indicator (OMI) based on ocean heat content (OHC) in the upper 300 m has also shown warming in the  
63 Black Sea. This increasing trend, as indicated by both reanalysis data and temperature measurements from Argo floats (Lima  
64 et al., 2020; Stanev et al., 2019), has contributed to the reduced presence of the CIL in the Black Sea in recent years.

65 Beyond OHC, Black Sea reanalysis has served as the foundation for other OMIs also produced within the scope of the  
66 Copernicus Marine Service. Using its velocity fields, Peneva et al. (2021) created an index for the Rim Current, showing that  
67 the annual mean current speed fluctuated by approximately 30% between 1993 and 2019, with a positive trend of about 0.1 m  
68  $s^{-1}$  per decade. Ilicak et al. (2022) analyzed the meridional overturning circulation in the Black Sea and identified a strong  
69 correlation between the CIL and a newly proposed index representing the maximum overturning circulation in density space.  
70 Gunduz et al. (2021) proposed an index to characterize the upwelling system along the Turkish coast. Their study revealed  
71 significant year-to-year variations in upwelling intensity and duration, driven primarily by wind patterns. In addition, they also  
72 found that recent declines in the CIL may have further influenced the properties of the upwelled waters.

73 Additionally, Black Sea reanalysis has played an important role in the practical development of the Black Sea physics forecast  
74 system (Ciliberti et al., 2022) and, more recently, in generating hourly datasets of velocity components and sea surface height  
75 for driving wave reanalysis within the framework of the Black Sea Monitoring and Forecasting Centre (BLK-MFC) under the  
76 Copernicus Marine Service (Ciliberti et al., 2021). One of the main challenges in developing a reanalysis for the Black Sea is  
77 the scarcity of in-situ observational data to be assimilated, particularly in certain periods, such as the 1990s. This data scarcity  
78 is even more pronounced in deeper layers. The absence of observational data requires the use of a robust model capable of  
79 accurately simulating the physical processes involved in the Black Sea. Thus, significant progress has been made in improving  
80 the quality of the BLK-REA model component with respect to its previous version, including the implementation of a new  
81 configuration with lateral open boundary conditions (LOBCs) to better simulate exchange flows through the Bosphorus Strait,  
82 such as the inflow of saltwater from the Marmara Sea. Also, the freshwater balance in the model has been refined by  
83 incorporating atmospheric forcing with hourly precipitation data, alongside monthly measurements of the Danube River  
84 discharge.

85 These improvements emphasize the importance of developing a regional reanalysis that integrates specific configurations and  
86 physical parameterizations tailored to accurately represent the unique characteristics of the Black Sea, which is challenging to  
87 achieve with global reanalyses. The latter often rely on fixed parameter adjustments optimized for other regions in the global  
88 ocean. In addition, a regional reanalysis typically utilizes higher-resolution models, allowing for a more accurate representation  
89 of mesoscale and submesoscale processes, which are often unresolved or only partially captured by the coarse resolution of  
90 current global reanalyses.

91 This article is organized as follows: Section 2 provides a detailed description of BLK-REA configuration, which was released  
92 in December 2024. Section 3 presents the main BLK-REA results and their validation, as well as the updated OMIs for the  
93 Black Sea based on BLK-REA. Finally, Section 4 summarizes the key findings and outlines improvements and data needs for  
94 future versions.

## 95 **2 Methodology**

96 Most of the methodology and configurations follow the previous Black Sea Reanalysis version (Lima et al., 2021), such that  
97 this section focuses on the main changes and enhancements present in the newly released version.

### 98 **2.1 Ocean Model**

99 The BLK-REA model component is the Nucleus for European Modelling of the Ocean (NEMO version 4.0, Madec and the  
100 Nemo team, 2019) configured for the domain (Azov and Marmara Seas are not included). NEMO is implemented at a  
101 horizontal resolution of  $1/40^\circ$  and 121 vertical geopotential levels. This horizontal resolution provides a spatial discretization  
102 of approximately 2.5 km, which conforms to the mesoscale eddy-resolving scale; the Rossby radius of deformation in the  
103 Black Sea is approximately 20 km. The model is driven by atmospheric fluxes derived from ECMWF ERA5 reanalysis with  
104 spatial and temporal resolutions of  $1/4^\circ$  and 1 hour, respectively. The atmospheric forcing considers the following variables:  
105 components of 10-m wind, total cloud cover, 2-m air temperature, 2-m dew point temperature, mean sea level pressure and  
106 precipitation. The system computes momentum, heat, and water fluxes at the air-sea interface using bulk formulae originally  
107 developed for the Mediterranean Sea (Castellari et al., 1998; Pettenuzzo et al., 2010), which have also been employed in other  
108 Black Sea systems (Ciliberti et al., 2022; Lima et al., 2021). Additionally, the system applies daily sea surface temperature  
109 relaxation for heat flux corrections based on the ESA-CCI SST-L4 product (Good et al., 2020).

#### 110 **2.1.1 Lateral open boundary conditions**

111 One of the key challenges in modeling the Black Sea dynamics is accurately simulating the outflow and inflow through the  
112 Bosphorus Strait. This is essential for correctly representing the surface and intermediate depth salinity patterns and sea surface  
113 height (SSH) trends, as the Bosphorus acts as the sole passage for saltwater entering the Black Sea, and the only exit of the  
114 surface Black Sea water. The previous Black Sea reanalysis approach applied closed boundary conditions, requiring  
115 temperature and salinity restoration to achieve more accurate results. Additionally, SSH was controlled by treating the  
116 Bosphorus as an inverse river with a controlled flow to prevent artificial SSH trends. The present version incorporates open  
117 boundaries, using results from the Unstructured Turkish Straits System (U-TSS) model (Ilicak et al., 2021), leading to a more  
118 accurate representation of these dynamics. U-TSS is built upon the Shallow Water Hydrodynamic Finite Element Model  
119 (SHYFEM; Micalletto et al., 2022). SHYFEM employs an unstructured finite element grid in the horizontal dimension and  
120 assumes hydrostatic approximation, solving depth-integrated shallow water equations in the vertical. The model features a  
121 horizontal resolution ranging from 500 meters in deeper regions to 50 meters in shallower areas, enabling a detailed  
122 representation of the Turkish Straits: Dardanelles and Bosphorus. Additionally, it incorporates 93 geopotential coordinate  
123 levels in the vertical dimension. The current reanalysis simulation utilizes LOBCs from monthly-averaged fields of  
124 temperature, salinity, U and V velocity components, and SSH from a 4-year U-TSS simulation covering the period 2016–2019.  
125 Flather’s boundary condition is applied to the barotropic component, while the flow relaxation scheme is utilized for tracers

126 and baroclinic components, as implemented in NEMO. Custom interfaces between U-TSS and BLK-REA have been developed  
127 to adapt the U-TSS model outputs for the BDY module in NEMO (Chanut, 2005).  
128 Due to computational constraints, the LOBCs at the Bosphorus Strait were derived from monthly-averaged outputs of a U-  
129 TSS simulation covering the period 2016–2019. A monthly climatology from this period was applied consistently over the full  
130 reanalysis timeline (1993–2022) to represent seasonal variability. Although this approach does not capture interannual signals  
131 at the boundary, the internal dynamics of the Black Sea, combined with the data assimilation of satellite and in situ  
132 observations, help maintain physical consistency throughout the basin.

## 133 **2.2 Observations**

134 The system assimilates sea level anomaly (SLA) data from the dataset European Seas Along-Track L3 Sea Surface Heights  
135 Reprocessed, Tailored for Data Assimilation, available in the Copernicus Marine Service catalog  
136 (SEALEVEL\_EUR\_PHY\_L3\_MY\_008\_061, <https://doi.org/10.48670/moi-00139>; Faugère et al., 2022). To maximize the  
137 number and spatial coverage of in-situ observations assimilated into the model, we combine multiple datasets using a  
138 predefined priority order, ensuring that duplicate profiles are excluded, as follows:

- 139 1. Global Ocean CORA In-situ Observations – Yearly Delivery in Delayed Mode from Copernicus Marine Service  
140 (INSITU\_GLO\_PHY\_TS\_DISCRETE\_MY\_013\_001; <https://doi.org/10.17882/46219>) (Szekely et al., 2024).
- 141 2. Global Ocean In-situ Near-Real-Time Observations from Copernicus Marine  
142 Service (INSITU\_GLO\_PHYBGCWAV\_DISCRETE\_MYNRT\_013\_030; <https://doi.org/10.48670/moi-00036>).
- 143 3. SeaDataNet historical in-situ data collections (Myroshnychenko and Simoncelli, 2018; Myroshnychenko, 2020).

144  
145 In data assimilation, the in situ instrumental errors assume different values for T and S and vary in the vertical dimension based  
146 on statistics derived from Ingleby and Huddleston (2007). The in-situ representation errors are defined as a multiplicative  
147 factor applied to the depth-dependent instrumental errors and vary horizontally on the model grid according to previous model-  
148 observation statistics. In this component, the same spatially varying factor is applied to T and S, which is a simplification  
149 justified by the similar spatial sampling patterns and statistical structure of the T/S in situ observational datasets. Representation  
150 errors account for unresolved physical processes, subgrid-scale variability, and model errors that are not part of instrumental  
151 uncertainties. Both components of in situ errors are kept constant over time. For SLA observations, the instrumental error is  
152 set to 4 cm, and the representation errors vary spatially and monthly following Oke and Sakov (2008). Similar to the previous  
153 version, a background quality check is implemented in the data assimilation system to reject observations that deviate  
154 significantly from the model prior solution. Rejection by background quality control does not necessarily indicate erroneous  
155 data, but often reflects large innovations that would otherwise introduce undesirable shocks in the model state. The quality  
156 control procedures and data rejection thresholds are applied as described in Lima et al. (2021), with no changes introduced in  
157 BLK-REA.

158 In contrast to the previous version of the reanalysis (Lima et al., 2021), which used a model-derived mean dynamic topography  
 159 (MDT), an enhancement in the present version is the use of an observation-based mean dynamic topography MDT to compute  
 160 the model-equivalent SLA in data assimilation. Sensitivity tests indicated that this choice improves the assimilation skill of  
 161 SLA, leading to systematically reduced RMSD values. The observation-based MDT field is available in the Copernicus Marine  
 162 Service catalog: <https://doi.org/10.48670/moi-00138>.

### 163 **2.3 Data Assimilation**

164 The data assimilation system, OceanVar, utilizes a three-dimensional variational (3D-Var) assimilation algorithm. OceanVar  
 165 was initially developed for the Mediterranean Sea (Dobricic and Pinardi, 2008) and subsequently extended to the global ocean  
 166 (Storto et al., 2011) and Black Sea (Ciliberti et al., 2022; Lima et al., 2021). The new system utilizes OceanVar, following the  
 167 same equations outlined in Lima et al. (2021), with particular emphasis on the cost function ( $J$ ) equation presented as follows:

$$168 \quad J = \frac{1}{2} \delta x^T B^{-1} \delta x + \frac{1}{2} (H \delta x - d)^T R^{-1} (H \delta x - d) \quad (1)$$

169 where  $\delta x = x_a - x_b$  is the increment, i.e., the difference between the analysis ( $x_a$ ) and background ( $x_b$ ),  $d = y - H(x_b)$  is  
 170 the misfit between an observation vector  $y$  and its modeled correspondent (in the observation space) where  $H$ , the observation  
 171 operator, maps the model fields to the observation locations. OceanVar is a multivariate scheme, i.e., the state vector  $x$  can  
 172 contain the following model state variables: T, S, SLA, and horizontal velocities (u and v). However, only the first three  
 173 variables are employed in the present BLK-REA implementation.  $B$  and  $R$  are respectively the background and observation  
 174 covariance matrices.  $R$  is diagonal in the observation space and includes the sum of instrumental and representation errors,  
 175 along with an additional error component that depends on the time difference between each observation and the analysis time.  
 176 The latter component is weighted according to this temporal distance.

177 In OceanVar, the variational cost function is solved using the incremental formulation (Courtier, 1997), with preconditioning  
 178 of the cost function minimization achieved through a change-of-variable transformation. Thus, to avoid inverting the  $B$  matrix  
 179 and to precondition the minimization of the cost function, the  $B$  matrix is defined as  $B = VV^T$  where  $V$  is decomposed into a  
 180 sequence of linear operators:  $V = V_\eta V_h V_v$ . The  $V$  operator represents the background error covariance matrix, capturing the  
 181 interdependencies among variables. Furthermore, a new control variable,  $v = V^+ x$  (and thereby  $x = Vv$ ), is introduced for the  
 182 minimization process through the application of a transformation. Thus Eq (1) becomes:

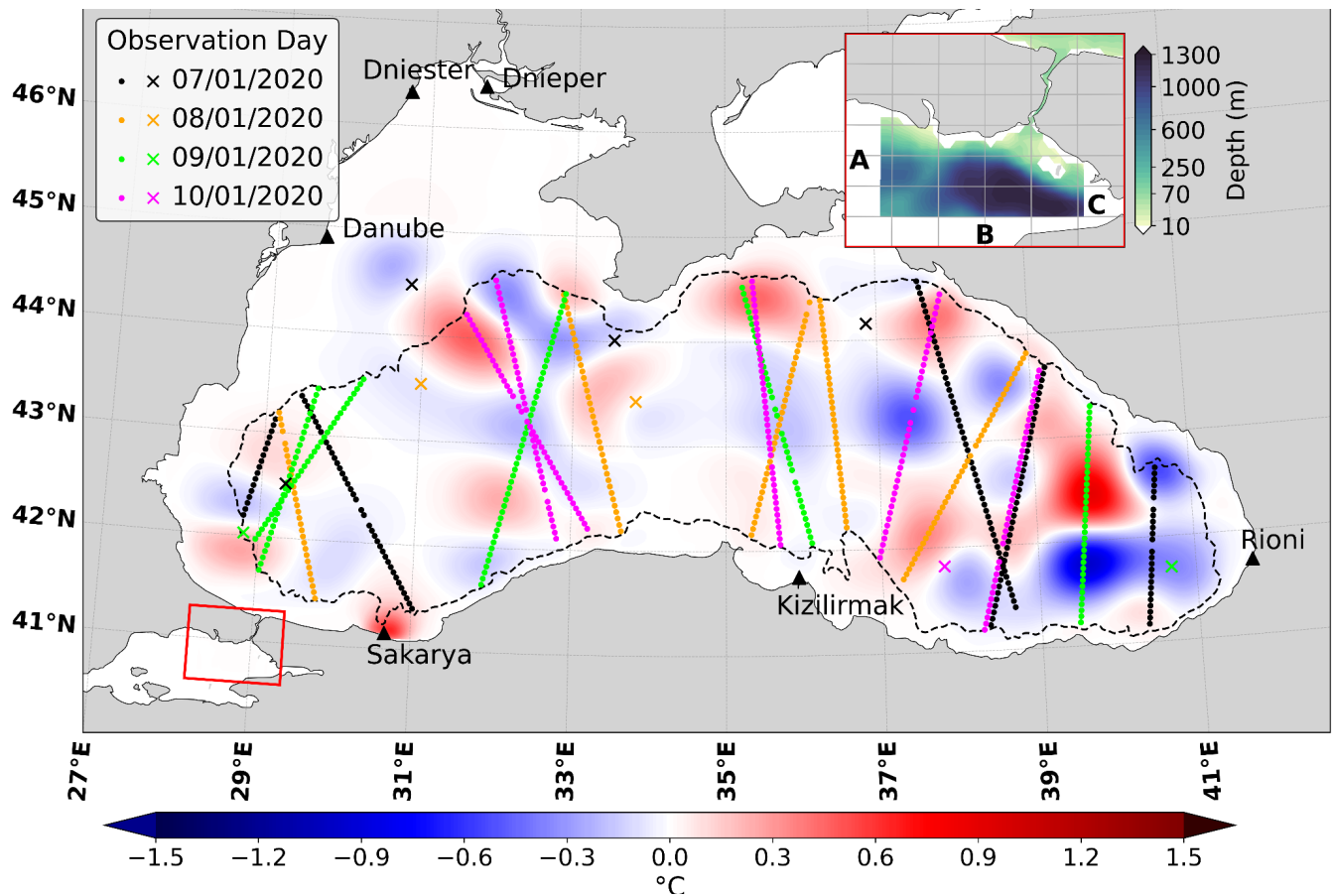
$$183 \quad J = \frac{1}{2} v^T v + \frac{1}{2} (HVv - d)^T R^{-1} (HVv - d) \quad (2)$$

184  
 185 In the present version, the linear operators  $V_\eta$  and  $V_h$  follow the same formulation described by Lima et al. (2021). The dynamic  
 186 height operator in  $V_\eta$  imposes local hydrostatic and geostrophic balance among SLA, temperature, and salinity increments,  
 187 following Storto et al. (2011), with a level of no motion assumed at 1000 m, where this balance is valid. This restricts SLA  
 188 assimilation to deep-water regions.  $V_h$  represents horizontal correlations, modeled with a first-order recursive filter (Farina et  
 189 al., 2015) and a fixed correlation length-scale of 20 km. Instead,  $V_v$  incorporates background-error T and S vertical covariances

190 that are modelled through 45-mode multivariate Empirical Orthogonal Functions (EOFs) and derives from a previous  
191 integration including the assimilation of SLA, T and S profiles, using the full model resolution. In addition, the new approach  
192 is non-stationary and a different set of EOFs are applied considering the following decades: 1984–1993, 1994–2003, 2004–  
193 2013, and 2011–2020. EOFs are calculated for each month from anomalies estimated from daily T, S and SSH fields with  
194 respect to the long-term monthly mean of the corresponding decade.

## 195 **2.4 Strategies and experiment setup**

196 The experiment is initialized in 1991 with a rest state of temperature and salinity fields derived from the World Ocean Atlas  
197 climatology (WOA 2018, Garcia et al., 2019). Following a spin-up of 2 years (1991-1992), the BLK-REA starts in 1993. The  
198 data assimilation is applied every 2 days, i.e., if the model initializes at time  $t$ , the next data assimilation cycle is performed at  
199 the time  $t + 2$ . The observation window is 4 days centered at the analysis time, so that each cycle assimilates observations  
200 from 2 days before until 2 days after the analysis time. Figure 1 shows SST increments (in °C) over the Black Sea on 09  
201 January 2020, overlapped with along-track SLA and in situ profile data assimilated during a single DA cycle in the BLK-REA.  
202 The subplot highlights the Marmara Box and its bathymetry, where boundary conditions from U-TSS are applied along faces  
203 A, B, and C. In the Black Sea, the limited availability of in-situ observations for assimilation leads to systematic errors in  
204 certain variables during specific periods, particularly in the deeper layers. To mitigate this bias, large-scale bias correction  
205 (LSBC) toward WOA2018 decadal climatologies is applied below 700 meters. The formulation and additional details on the  
206 LSBC scheme are described in Lima et al. (2021).



207  
208  
209  
210  
211  
212  
213

Figure 1: SST increments (in °C) over the Black Sea on 09 January 2020, shown with a blue–white–red color scale. Triangles mark the positions of the main river inflows, while along-track SLA observations and in situ profile data (mostly Argo floats during this period; showing their positions as ×) are also displayed. Each color corresponds to a different day within a 4-day observation window centered at 00:00 UTC on 09 January 2020. The subplot highlights the Marmara Box (red rectangle) and its corresponding bathymetry, where boundary conditions from U-TSS are prescribed along faces A, B, and C. No assimilation is performed inside the Marmara Sea, and thus the SST increments there are zero.

214

### 3 Results and discussion

215  
216  
217

This section presents validations of key variables from the BLK-REA. The validations are quasi-independent, as they consider both assimilated observations and those excluded during the data assimilation process due to specific adjustments (e.g., background quality control). Additionally, it provides results for a set of OMI s computed from the BLK-REA.

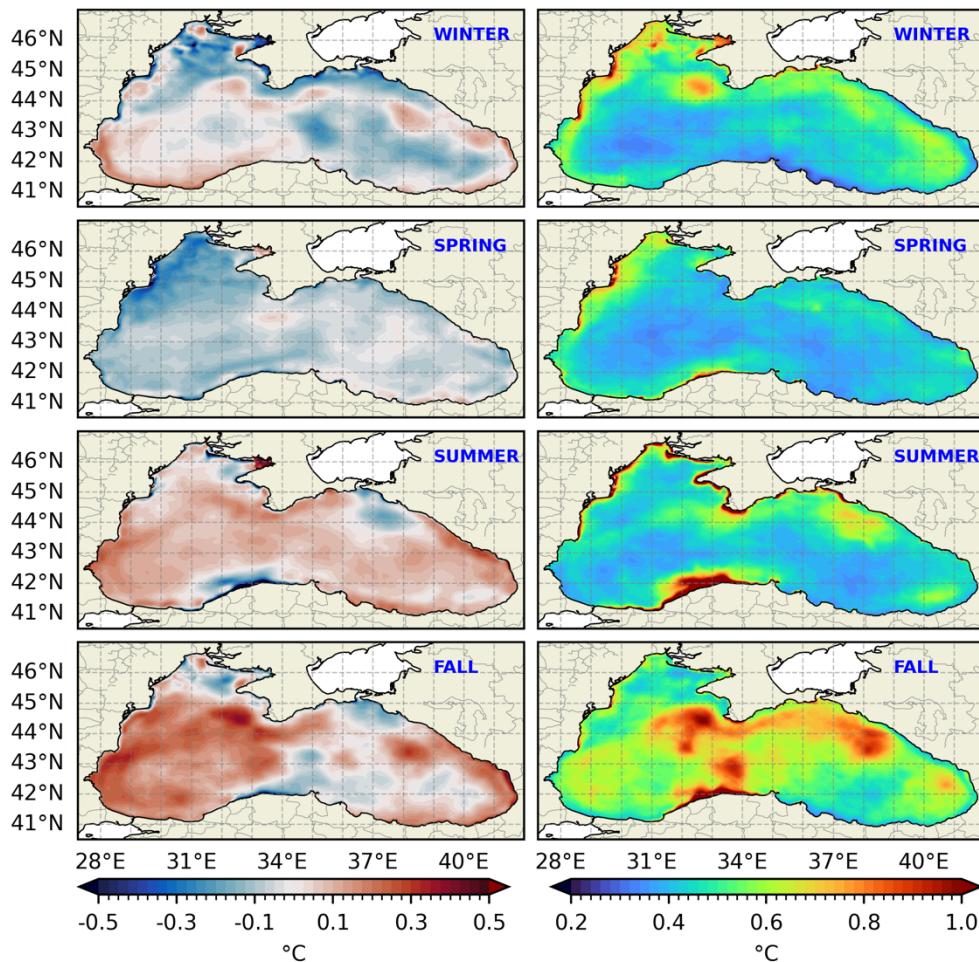
218

#### 3.1 Validation

219  
220  
221

Spatial seasonal maps of reanalysis SST are compared to satellite data in the period 1993-2022 and their difference shows a predominance of model negative biases in winter and spring, and positive biases in summer and fall, with a few exceptions as follows (Figure 2; left). Positive values of 0.1°C up to 0.3°C are visible in some regions during winter, such as close to the

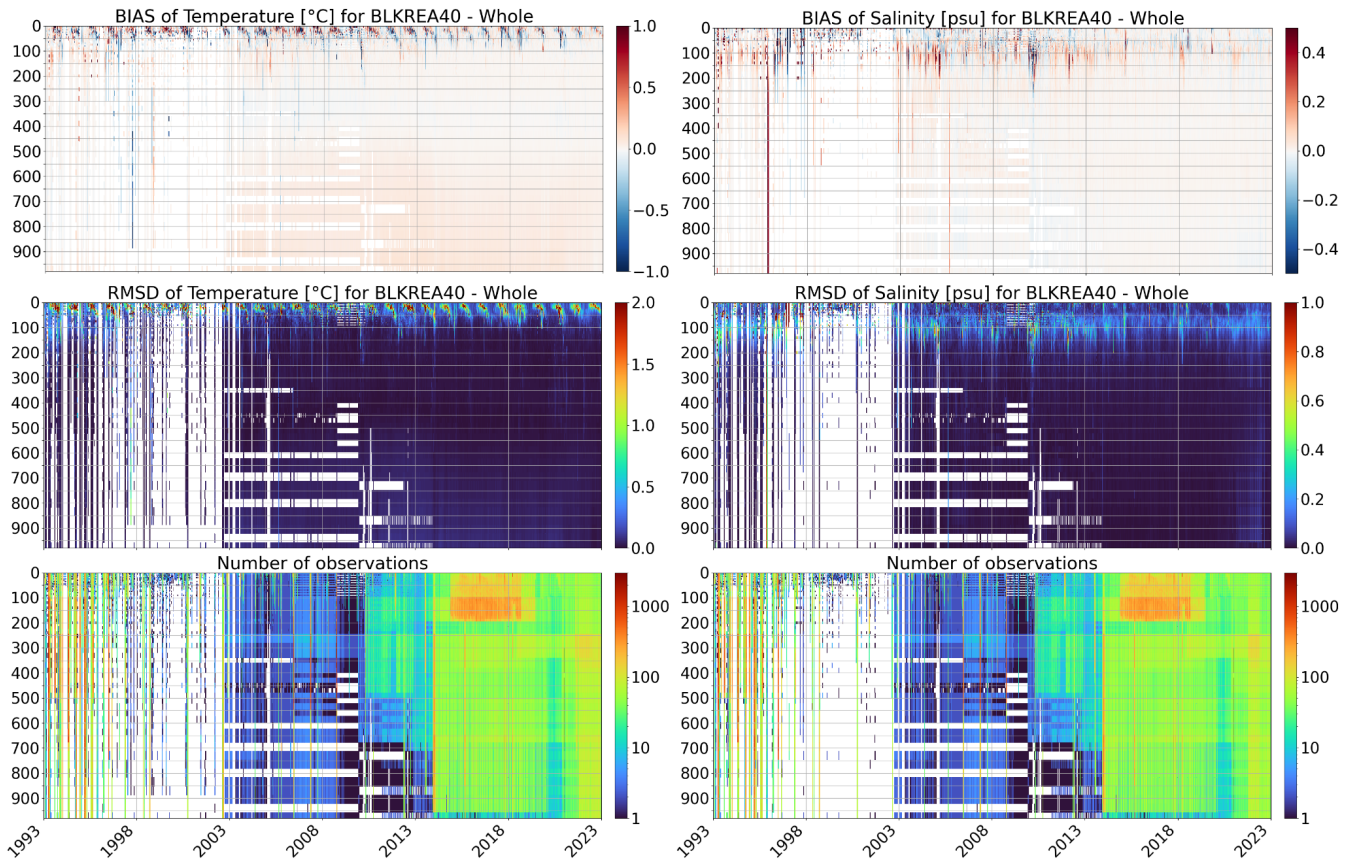
222 Danube river mouth and along the southwest coast. Negative biases are present adjacent to the Kerch Strait, and the lowest  
 223 negative biases, of more than  $1.0^{\circ}\text{C}$ , are exhibited in the upwelling region along the western Anatolian coast in summer. Most  
 224 of the central-eastern area is covered by negative bias in fall. SST RMSD (Root Mean Squared Difference) maps indicate that  
 225 errors are generally lower in spring and higher in fall (Figure 2; right). In general, larger values can be seen close to large river  
 226 mouths such as near the Dnieper in winter and Danube in winter, spring, and summer. The highest errors, exceeding  $1^{\circ}\text{C}$ , are  
 227 observed along the western Anatolian Turkish coast in both summer and fall. In this region, a similar overestimation of  
 228 upwelling phenomena was observed in the results of the previous Black Sea reanalysis, which was attributed to the influence  
 229 of stronger winds (Lima et al., 2021). Recent analyses have indicated that the air-sea bulk formulation may be responsible for  
 230 the intensified upwelling, and we plan to refine this model component in future releases of the Black Sea reanalysis.



231  
 232 **Figure 2: Seasonal maps of the mean bias (left) and RMSD (right) of the SST ( $^{\circ}\text{C}$ ) with respect to the satellite ESA-CCI product**  
 233 **over the period between 1993 and 2022. From top to bottom: winter, spring, summer, and fall.**

234

235 The Hovmöller diagram (time–depth) of RMSD for temperature computed as a lateral average, reveals a distinct seasonal cycle  
 236 in the upper water column (Figure 3), with lower errors in winter that increase during summer, exceeding 2°C in the upper 50  
 237 meters. This summer increase is associated with the model's misrepresentation of the seasonal thermocline, which is partially  
 238 corrected through data assimilation. Below 100 m, errors remain low, staying below 0.25°C for almost the whole period.  
 239 Before the Argo floats era (mid-to-late 2000s), the scarcity of in-situ data limited the effectiveness of data assimilation,  
 240 compromising both the model correction and the validation process.  
 241



242  
 243 **Figure 3** : Hovmöller (time–depth) diagrams of temperature (left) and salinity (right) in the Black Sea from 1 January 1993 to 31  
 244 December 2022. Rows show bias (top), RMSD (middle), and number of observations (bottom). Temperature is in °C and salinity in  
 245 PSU.

246 The Hovmöller diagram of temperature biases predominantly shows positive values, occasionally exceeding 1°C near the  
 247 surface, with intermittent periods of negative biases (Figure 3). The most pronounced discrepancies are observed within the  
 248 seasonal thermocline depths. There is a tendency for biases to shift from positive in upper layers to negative values at deeper  
 249 layers, down to 100 m. This may be related to the misrepresentation of the vertical position of the seasonal thermocline in the  
 250 BLK-REA results compared to observations over time.

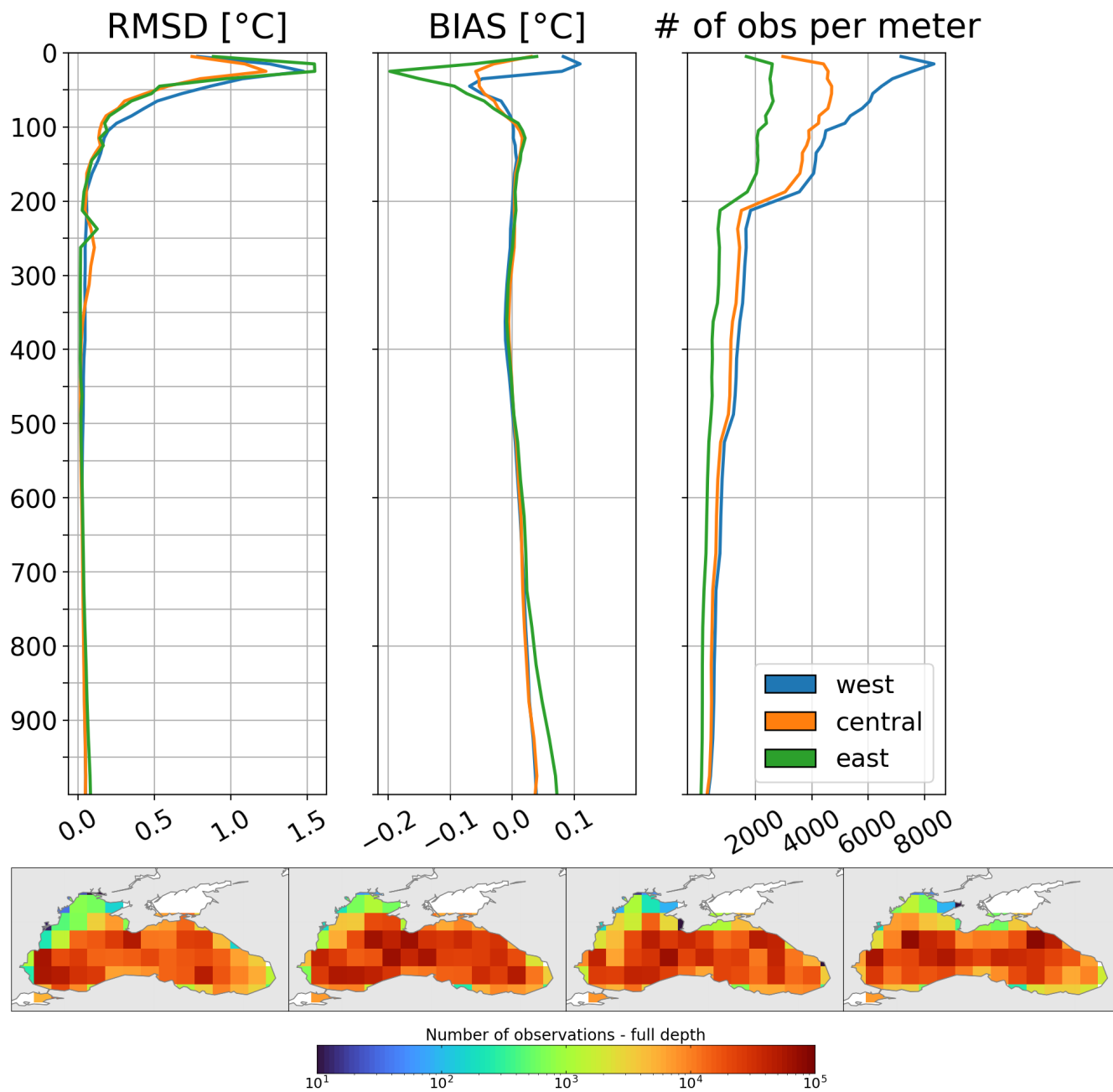
251 Unlike temperature, the Hovmöller diagram of RMSD for salinity does not exhibit a clear seasonal cycle. Errors exceed 1 psu  
252 during short periods (Figure 3), particularly in the upper layers, where high uncertainties are likely derived from precipitation  
253 biases in ERA5, simplified river runoff forcing, and the internal freshwater budget computed via the model's bulk formulae.  
254 Apart from these peak values, errors are relatively higher between 50 and 100 m. Within this layer, errors tend to decrease  
255 over time, reaching values below 0.25 psu in the most recent years of validation. Once again, the scarcity of observations  
256 compromises the validation process before 2004. Below 200 m, errors remain very low, with values consistently below 0.1  
257 psu.

258 Salinity biases show a predominance of positive values (Figure 3). The Hovmöller diagram reveals two main characteristics:  
259 BLK-REA diverges more from observations in the upper 200 m, with values alternating between positive and negative biases.  
260 Below 200 m, biases approach zero and remain predominantly positive. Since 2014, the values tend to be closer to zero, with  
261 biases showing a relative reduction in the upper 200 m.

262 During the validation stage, the elevated T/S errors around 1996 (salinity) and 1998 (temperature) in the Hovmöller diagrams  
263 (Figure 3) may be linked to observations that were not assimilated but included in the quasi-independent validation. These  
264 peaks are likely due to such observations, but also sparse coverage, and local model biases.

265 Figure 4 presents the temporal and spatial averaged RMSD and biases for temperature, comparing the reanalysis results with  
266 in-situ observations. For a better spatial analysis, we divide the Black Sea into three different regions: western, central, and  
267 eastern. The largest temperature errors occur in the upper layers and are primarily associated with the formation of the seasonal  
268 thermocline in summer, as previously shown in the Hovmöller diagrams for temperature (Figure 3). In this layer, RMSD  
269 reaches a maximum of approximately 1.5 °C in the western and eastern regions, and about 1.25 °C in the central region. In the  
270 upper water column, temperature biases are negative in the eastern and central regions. In the western region, the bias is  
271 positive from the surface down to 50 meters, reaching values of up to 0.1 °C, and becomes negative between 50 and 100  
272 meters, aligning with the values observed in the central region. The largest errors are observed in the eastern region. Errors  
273 gradually decrease with depth, with RMSD reaching values lower than 0.25°C at 150 m, biases becoming closer to zero.

274



275

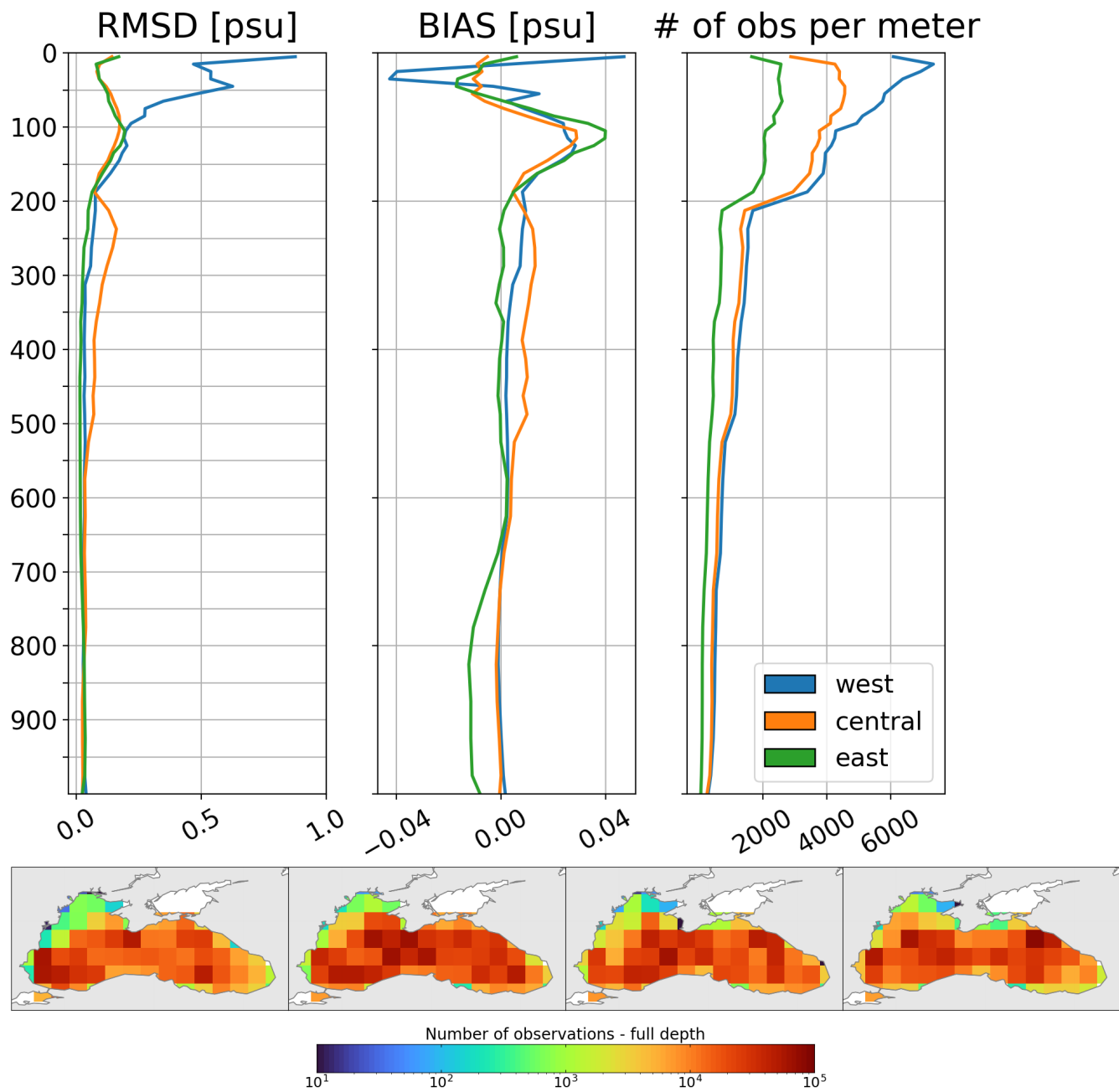
276 **Figure 4: Vertical profiles of the RMSD (left panel), bias (middle panel) and number of observations (right panel) for temperature**  
 277 **(in °C), by comparing the reanalysis results against in-situ profilers in three areas (West, Central and East) of the Black Sea domain**  
 278 **from 1 January 1993 to 31 December 2022. Seasonal spatial maps at the bottom show the total number of temperature observations**  
 279 **throughout the entire water column, from left to right: winter, spring, summer, and fall.**

280

281 The same analysis for salinity is shown in Figure 5. The western region exhibits the highest near-surface RMSD, with values  
282 reaching over 0.8 psu in the upper 100 m, despite high observational coverage. In contrast, RMSD values are lower in the  
283 central and eastern regions, remaining below 0.2 psu in the upper layers. These high values in the western region are mainly  
284 due to limitations in freshwater inputs from major rivers: only the Danube uses monthly varying discharge, while other rivers  
285 follow climatologies without intra-annual variability, producing persistent local biases. Prescribed boundary conditions near  
286 the Bosphorus Strait improve the physical representation but also introduce uncertainties. Data assimilation can partially  
287 improve model representation under these circumstances by incorporating observations with strict quality control, but some  
288 errors can still persist. Salinity biases show regional differences. In the western region, positive biases are pronounced near the  
289 surface, rapidly transitioning to negative values and reaching about  $-0.04$  psu between 25 and 50 m. In contrast, biases in the  
290 surface layers of the central and eastern regions remain closer to zero but increase in the subsurface starting at 50 m, following  
291 the pattern observed in the western region. At a depth of around 100 meters, all regions exhibit relatively high salinity biases,  
292 with the eastern region showing the highest values, reaching up to 0.04 psu. In general, salinity biases decrease beneath 100  
293 meters and approach zero at depths greater than 200 meters.

294 In the Eastern region, a slight increase in temperature and salinity biases occurs below 700 m (Figures 4 and 5). This pattern  
295 likely arises from sparse deep-layer observations prior to 2003 (as shown in the Hovmöller diagrams, Figure 3), limitations in  
296 model initialization, and unresolved physical processes within the model. The introduction of Argo profiling floats from 2003  
297 increased deep data coverage, revealing biases that were previously undetected and never corrected; below 700 m, LSBC  
298 toward WOA2018 climatology is not sufficient to constrain the model. In addition, some observations excluded from  
299 assimilation were still included in validation, further contributing to the apparent increase in errors. Even with strict quality  
300 control, some measurement errors or inconsistencies may have persisted.

301



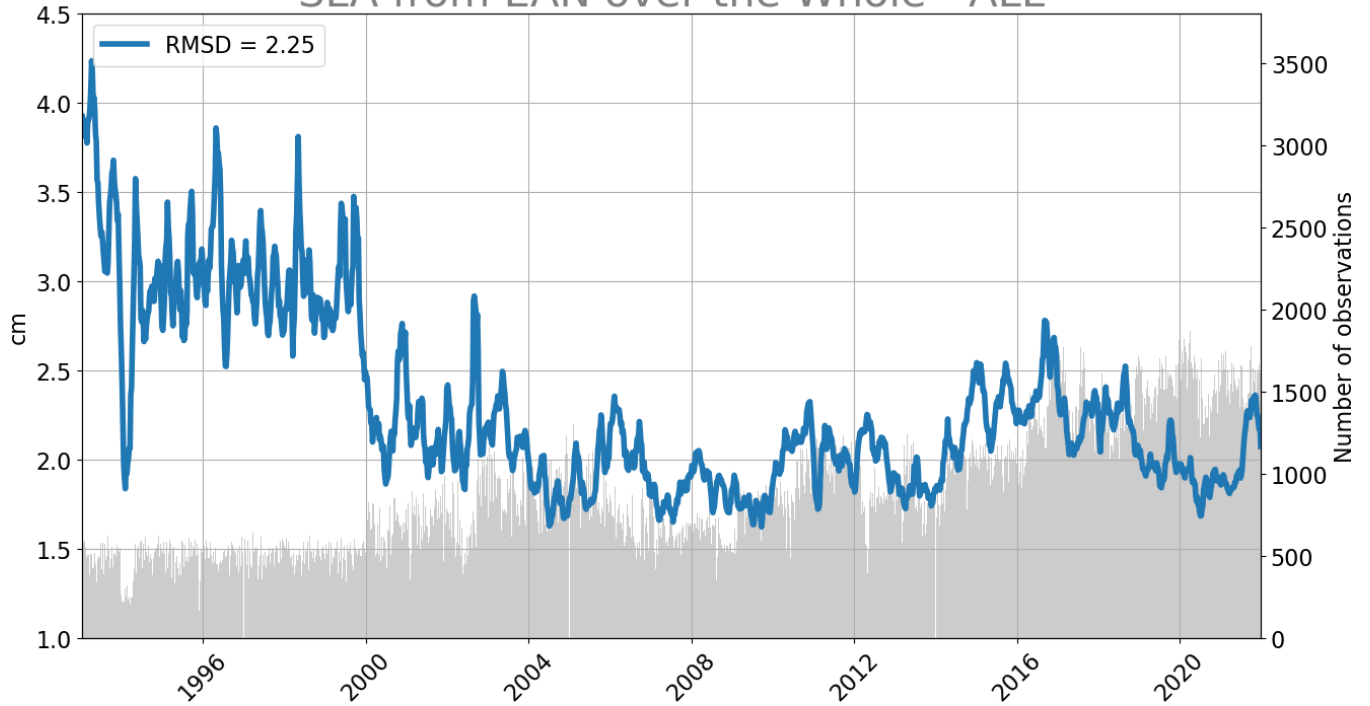
302

303 **Figure 5: Vertical profiles of the RMSD (left panel), bias (middle panel) and number of observations (right panel) for salinity (psu),**  
 304 **by comparing the reanalysis results against in-situ profilers in three areas (West, Central and East) of the Black Sea domain from 1**  
 305 **January 1993 to 31 December 2022. Seasonal spatial maps at the bottom show the total number of salinity observations throughout**  
 306 **the entire water column, from left to right: winter, spring, summer, and fall.**

307

308 The time series of spatially averaged SLA RMSD (Figure 6) shows strong skill after 2000, with errors around 0.02 m, below  
309 the instrumental error of 0.04 m used in assimilation. This improvement reflects the increased availability of satellite altimetry,  
310 while in situ T/S profiles remained scarce, making SLA the main constraint on the model. Instead, the slight RMSD increase  
311 around 2016 coincides with the larger availability of Argo profiles. Their assimilation, together with SLA, may have slightly  
312 degraded SLA skill due to the multivariate nature of the system. Nevertheless, the RMSD remains well within acceptable  
313 limits, and these points are intended to provide an overview of SLA performance rather than a detailed attribution of small  
314 temporal fluctuations. It is to be noted that the evaluation is performed in areas deeper than 1000 m, considered as the level of  
315 no motion when assimilating SLA data through a dynamic height operator. Spatial maps of the sea level anomaly RMSD reveal  
316 the highest values, ranging from 2.5 to 4 cm, with occasional peaks exceeding 4 cm, predominantly along the basin's periphery  
317 (Figure 7). These elevated deviations are closely linked to the Rim Current and its inherent mesoscale variability. In contrast,  
318 SLA RMSD values in the central basin are generally lower, around 2 cm. Notably, areas with large RMSD values align with  
319 regions of strong eddy kinetic energy (EKE), which we use to assess mesoscale activity (Figure 8). This pattern is particularly  
320 evident along the Anatolian, Caucasian, and Crimean coasts, where well-known mesoscale characteristics are present  
321 (Koroatev et al., 2003). SLA errors show slight variations across seasons, with particular attention given to high values along  
322 the Caucasian coast. These values extend further offshore in winter. Additionally, higher SLA errors occupy a larger area  
323 around the Batumi eddy region during fall. Error values are relatively high along the Crimean coast, particularly in the western  
324 region, where the persistent influence of the Sevastopol eddy contributes to elevated mesoscale variability. However, these  
325 errors tend to decrease during summer. Kubryakov and Stanichny (2015) reported that the total number of detected eddies  
326 exhibits local maxima in both the Sevastopol and Batumi eddy regions, reflecting the dynamic nature of coastal circulation in  
327 these areas. These complex dynamics may not be adequately resolved by the model, potentially contributing to elevated SLA  
328 errors in these areas.

## SLA from EAN over the Whole - ALL

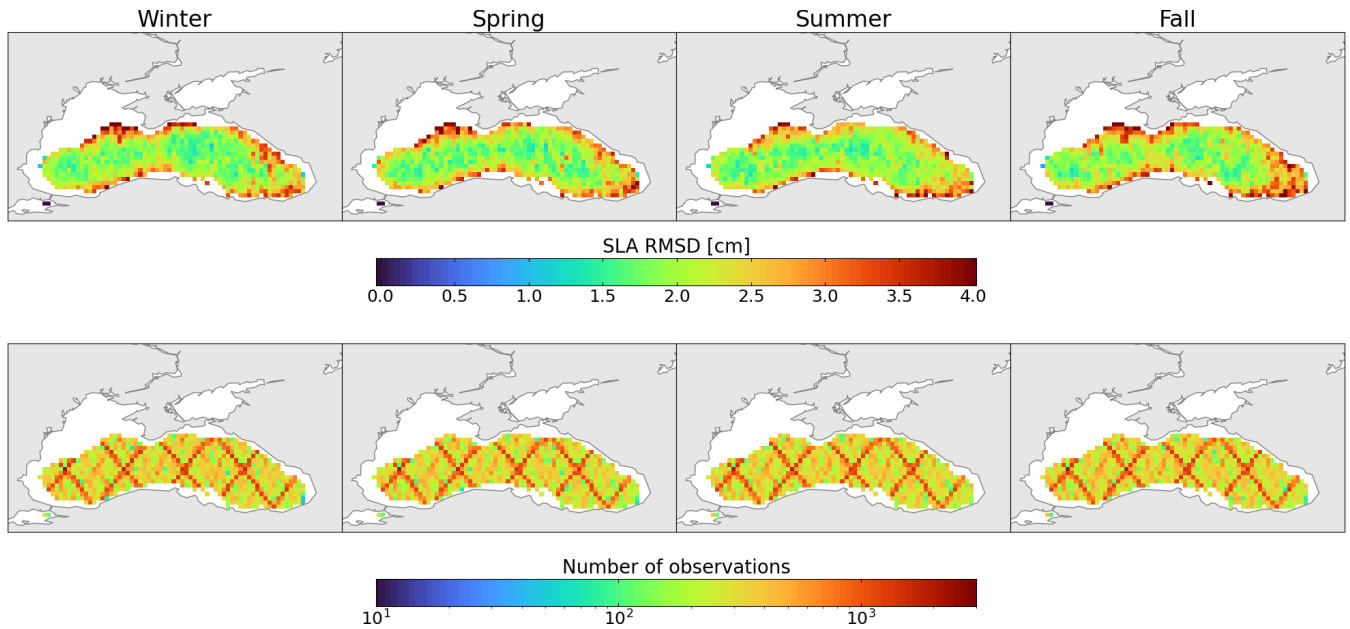


329

330

331

**Figure 6: Time evolution of basin-averaged SLA RMSD, comparing BLK-REA with satellite along-track SLA data, with a 7-day moving average applied to smooth short-term variability.**



332

333

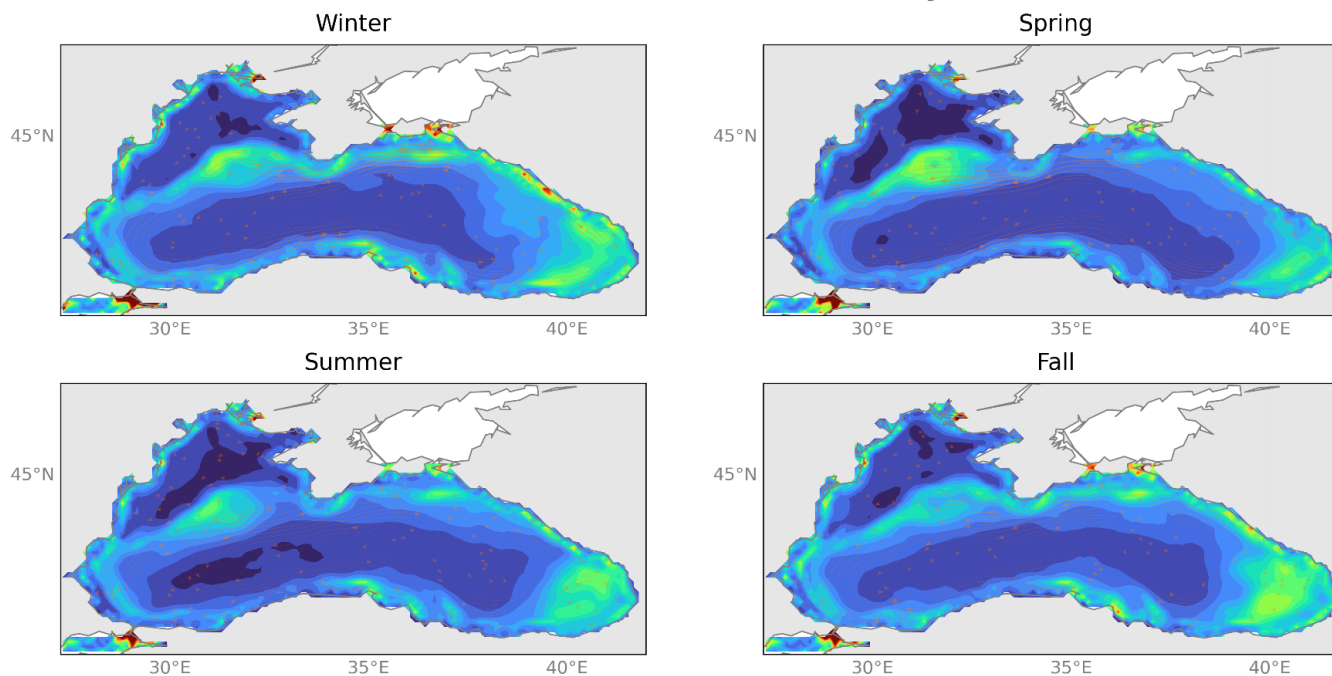
334

**Figure 7: Seasonal maps of the mean RMSD (top) of the SLA (cm) with respect to the satellite along-track SLA product over the period between 1993 and 2022. Bottom maps indicate the number of observations for each season.**

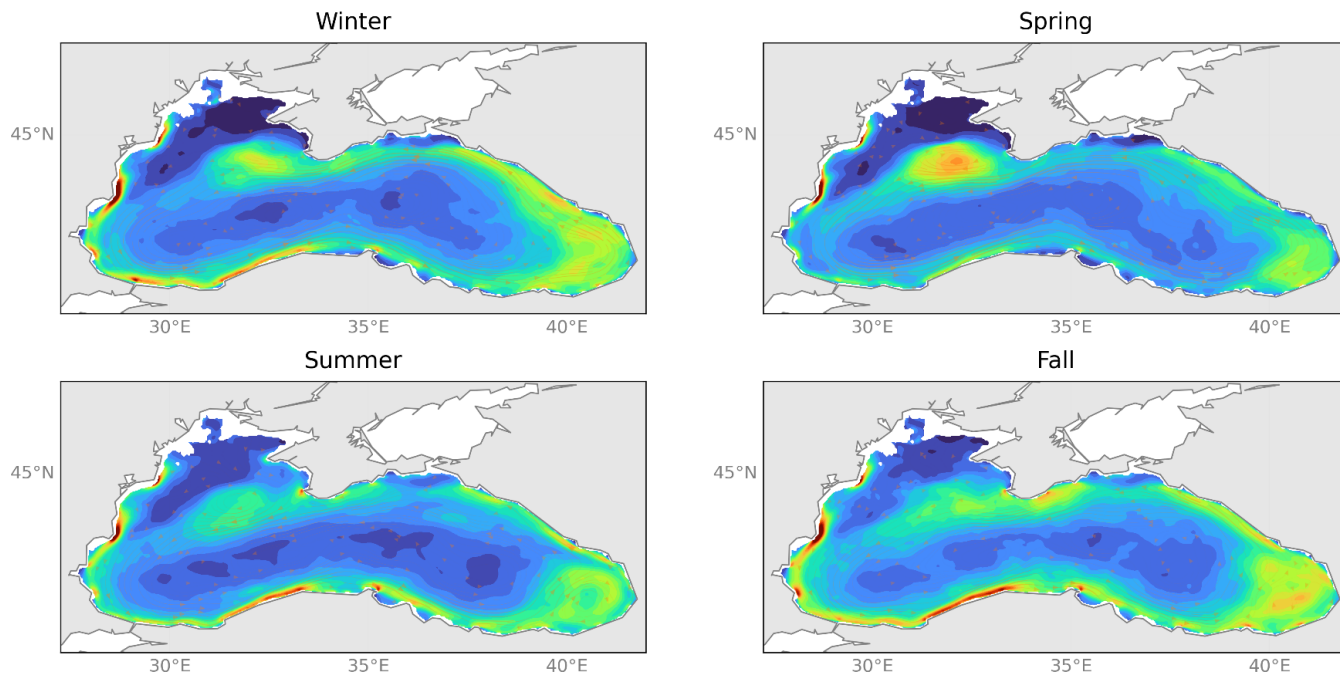
335 This interpretation is further supported by EKE maps (Figure 8), which consistently show high energy levels in these regions,  
336 indicating intense mesoscale activity that aligns with the SLA discrepancies viewed in Figure 7. EKE maps show elevated  
337 values along the Rim Current, particularly along the Caucasian coast. To ensure a clean comparison with altimetry-derived  
338 estimates, BLK-REA EKE was computed from the geostrophic component only, using SSH from the model. BLK-REA EKE  
339 values generally exceed those derived from altimetry, especially in the Batumi and Sevastopol eddies, where peak values reach  
340 about  $300 \text{ cm}^2 \text{ s}^{-2}$  in fall and spring, respectively, compared to altimetry-based estimates of around  $220 \text{ cm}^2 \text{ s}^{-2}$ . This difference  
341 likely reflects multiple factors, including the spatial smoothing inherent to the  $0.25^\circ$  Level-4 altimetry product, the reduced  
342 capability of altimetry to capture smaller-scale variability due to mapping and interpolation procedures, and possible over-  
343 energetic behaviour of the model arising from its higher resolution, physical parameterizations, and potentially insufficient  
344 dissipation of mesoscale energy.

345

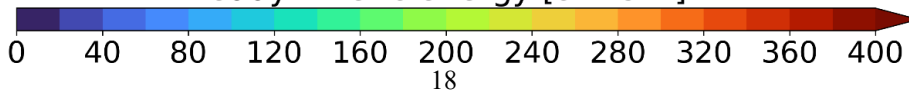
# seasonal EKE from altimetry



# BLKREA40 seasonal EKE



eddy kinetic energy [ $cm^2s^{-2}$ ]



347

348 **Figure 8: Seasonal maps of eddy kinetic energy (EKE) ( $\text{cm}^2 \text{s}^{-2}$ ) from satellite SLA L4-product and BLK-REA over the period**  
349 **between 1993 and 2022, based on the surface geostrophic velocity component.**

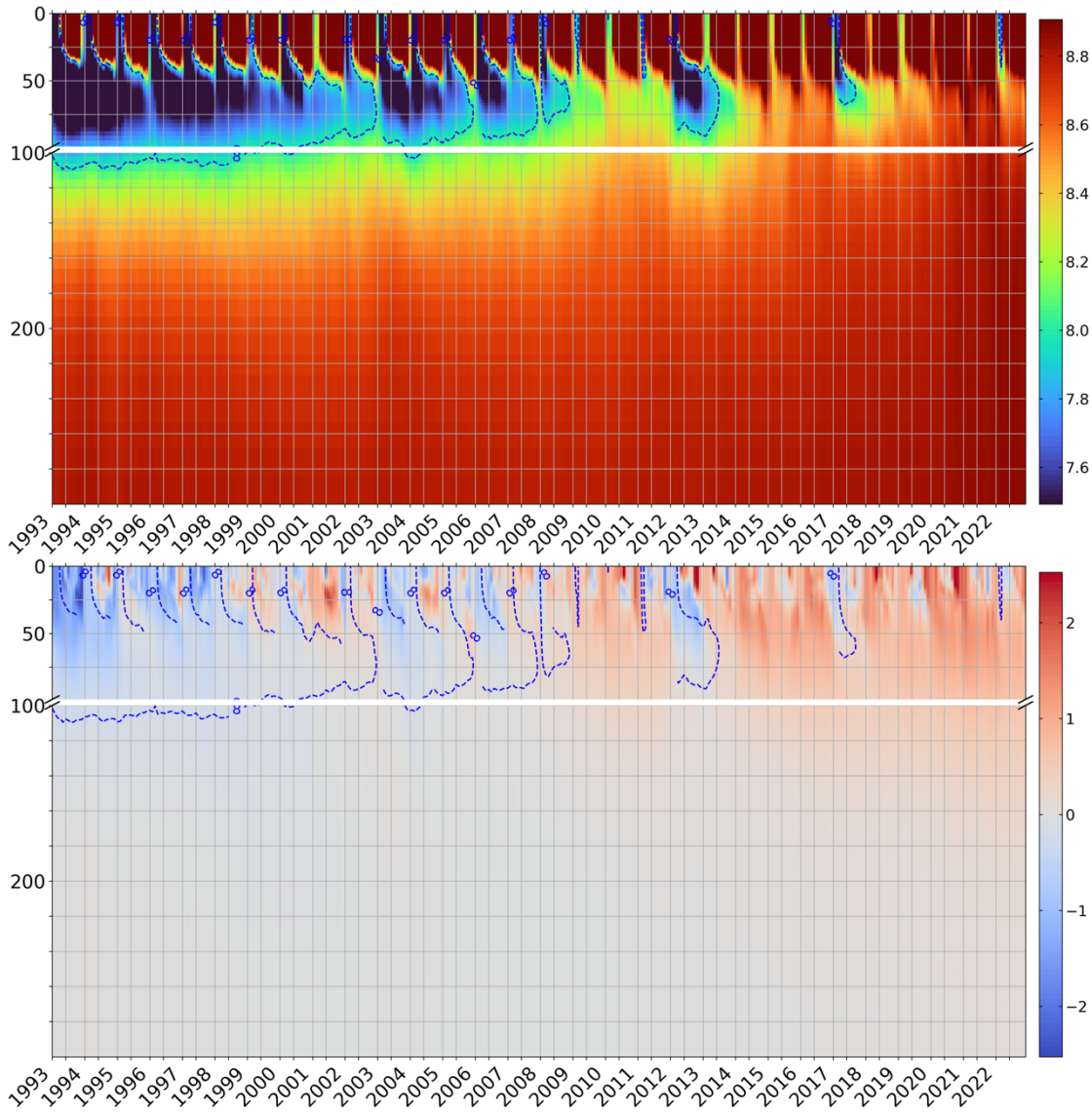
350

## 351 **3.2 Ocean monitoring indicators**

352 We present a set of OMIs computed from the BLK-REA: ocean heat content, Rim Current interannual variability, and  
353 meridional overturning circulation. These indicators provide valuable insights into key aspects of Black Sea dynamics.

### 354 **3.2.1 Ocean heat content**

355 Figure 9 illustrates the time evolution of basin-averaged temperature, with the 8 °C isotherm selected to track the Black Sea  
356 CIL over time. The formation of the CIL is mainly associated with water cooling during the winter season, and its presence is  
357 consistently observed until 2008. From 1993 to 2008, the CIL extends from the surface to approximately 100 meters in depth.  
358 After 2008, this pattern exhibits a significant shift, as temperatures rise, leading to the frequent disappearance of the CIL.  
359 Nevertheless, instances of CIL formation are also observed in 2012, with a reduced extent in 2017, consistent with Argo float  
360 measurements (Stanev et al., 2019). More recently, a very weak CIL formed in March 2022, as documented by Çokacar et al.  
361 (2024), who attributed this event to intense cold-air masses that caused severe weather conditions across southern Europe,  
362 including the Black Sea, and influenced CIL formation.



363  
 364 **Figure 9: Hovmöller (time-depth) diagrams of monthly basin-averaged temperature in °C (top) and anomaly of temperature in °C**  
 365 **(bottom). The monthly anomaly estimates considered the climatological period 1993–2014 of each corresponding month. The blue**  
 366 **dashed line indicates the mean position of the 8°C isotherm (top).**

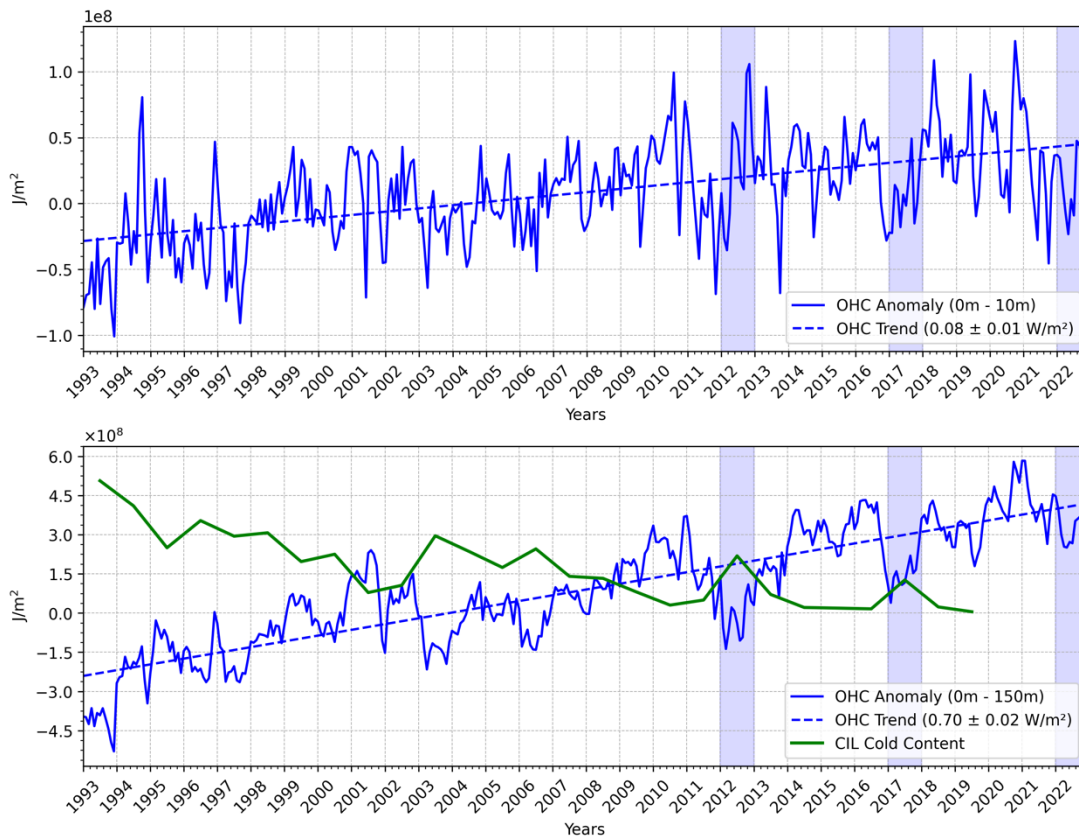
367 The warming signal is evident in the Hovmöller diagram of temperature anomalies, which shows a predominance of positive  
 368 values starting in 2009. Occasionally, positive values are interrupted by negative anomalies in the upper layers, as seen in years  
 369 with the presence of the CIL: 2012, 2017, and 2022.

370 The analysis of ocean heat content in the Black Sea follows the formulation outlined by Lima et al. (2020), as described by the  
 371 equation below:

372 
$$OHC = \int_{z_1}^{z_2} \rho_0 c_p (T_m - T_{clim}) dz \quad (3)$$

373 with  $\rho_0$  equal to  $1020 \text{ kg m}^{-3}$  and  $c_p$  equal to  $3980 \text{ J kg}^{-1}\text{C}^{-1}$  are, respectively, the density and specific heat capacity; and  $dz$   
374 indicates a certain ocean layer limited by the depths  $z_1$  and  $z_2$ ;  $T_m$  corresponds to the monthly averaged temperature and  $T_{clim}$   
375 is the climatological temperature of the corresponding month. In this study, OHC is calculated as the deviation from the  
376 reference period of 1993–2014.

377 The OHC in both the 0-10 m and 0-100 m layers shows an overall warming trend, with values of  $0.08 \text{ W m}^{-2}$  and  $0.59 \text{ W m}^{-2}$ ,  
378 respectively (Figure 10). Table 1 shows OHC trends within other layers to compare the values with those reported by Lima et  
379 al. (2021), who analyzed OHC trends using the previous Black Sea reanalysis (Lima et al., 2021) during the period 1993–  
380 2018. In general, the newest BLK-REA shows lower OHC trends. In the 0-10 m layer, the OHC curve shows several positive  
381 peaks around  $1 \times 10^8 \text{ J m}^{-2}$  in 2010, 2012, 2018, and 2020. In contrast, negative peaks are observed in 1993, 1997, and 2001.  
382 An interesting observation is that although the CIL is present in 2012, there are positive anomalies in the upper layers that  
383 year. This suggests that colder waters from the upper layers, which subducted in 2011, may have reached the CIL levels in  
384 2012. These features are visible in the Hovmöller diagrams of basin-averaged temperature anomalies (Figure 9). The CIL  
385 signal is clearly present in the 0-100 m layer in 2012. Additionally, the OHC shows a clear agreement with the CIL cold content  
386 observed in the data, which was estimated by Capet et al. (2020) using temperature observations from various platforms.  
387 Specifically, years of higher heat content correspond to a reduction in CIL cold content, while years of lower heat content  
388 coincide with an increase in CIL cold content. In more recent years, the CIL cold content values are nearly zero, except for  
389 2012 and 2017, when the values exceeded  $1.5 \times 10^8 \text{ J m}^{-2}$  in 2012 and were slightly below this threshold in 2017; see the green  
390 curve in Figure 10. Correspondingly, both years show a decrease in OHC, reinforcing the relationship between CIL cold  
391 content and heat content variability.



392

393 **Figure 10: Monthly basin-averaged of the ocean heat content anomalies (in  $J m^{-2}$ ) estimated for the BLK-REA in 0-10 m (top) and**  
 394 **0-100 m (bottom). The monthly ocean heat content anomalies are defined as the deviation from the climatological ocean heat content**  
 395 **mean (1993–2014) of each corresponding month. Mean trend values are also reported for each layer (bottom right corner). In 0-100**  
 396 **m (bottom), the green curve corresponds to the CIL cold content from Capet et al. (2020). The blue shades highlight the recent years**  
 397 **when the CIL is present: 2012, 2017 and 2022.**

398

399 **Table 1: Trends estimations together with the 95% confidence interval (in brackets) for the ocean heat content anomaly ( $W m^{-2}$ )**  
 400 **from BLK-REA for the periods 1993–2022 and 1993–2018, and from the previous Black Sea reanalysis (Lima et al., 2021) for the**  
 401 **period 1993–2018.**

	1993-2022	1993-2018	
	BLK-REA	BLK-REA	Lima et al. (2021)
0-10 m	0.08 (0.01)	0.09 (0.01)	0.11 (0.01)
0-50 m	0.35 (0.02)	0.37 (0.02)	0.45 (0.04)
0-200 m	0.74 (0.02)	0.72 (0.03)	0.81 (0.05)
0-1000 m	0.84 (0.02)	0.83 (0.03)	0.83 (0.04)

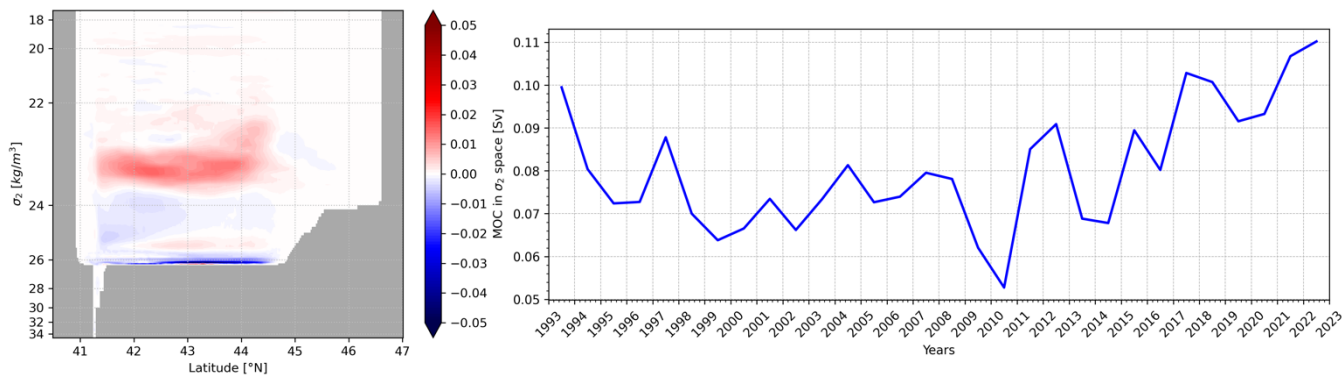
402  
403

### 404 3.2.2 The Black Sea overturning circulation

405 We follow the methodology of Ilicak et al. (2022), computing the meridional overturning circulation (MOC) in density space  
406 to better represent water mass transport in the Black Sea. We divide the water mass structure of the Black Sea in 50 different  
407 sigma2 ( $\sigma_2$ ; potential density anomaly with [ $\text{kg m}^{-3}$ ] respect to a reference pressure of 2000 dbar) density bins and compute  
408 the MOC using the formula:

$$409 \psi^*(y, \bar{\sigma}) = -\frac{1}{T} \int_{t_0}^{t_1} \int_{x_{B1}}^{x_{B2}} \int_{-H}^0 H[\bar{\sigma} - \sigma(x, y, z, t)] \times v(x, y, z, t) dz dx dt \quad (4)$$

410 where  $H$  is the Heaviside function and  $v$  is the meridional velocity. We used 100  $\sigma_2$  density bins to remap the mass flux fields.  
411 A very narrow cell with positive values (clockwise circulation) of approximately 0.03–0.04 Sv is observed just below 26  $\text{kg m}^{-3}$   
412  $\text{m}^{-3}$  around 43°N (Figure 11). However, at densities higher than 26  $\text{kg m}^{-3}$ , the MOC structure predominantly exhibits negative  
413 values (indicative of anticlockwise circulation), exceeding -0.03 Sv. At a density of approximately 25.5  $\text{kg m}^{-3}$ , the MOC  
414 forms a dipole pattern, with slightly positive values between 42°N and 44.5°N and negative values south of 42°N. Above this,  
415 the circulation remains anticlockwise until approximately 23.75  $\text{kg m}^{-3}$ , where a clockwise pattern re-emerges between 23.75  
416  $\text{kg m}^{-3}$  and 22  $\text{kg m}^{-3}$ , with positive transport exceeding 0.02 Sv. Nonetheless, within this layer, localized negative values are  
417 observed, particularly around 45°N. In general, below 23.75  $\text{kg m}^{-3}$ , there is a predominance of anticlockwise circulation,  
418 especially in the southern part of the basin, likely associated with the inflow of Mediterranean Water into the Black Sea. Above  
419 this isopycnal, positive values indicate a clockwise circulation, which is linked to the formation of the CIL. These findings are  
420 consistent with the results of Ilicak et al. (2022).



421  
422 **Figure 11: Time-mean overturning transport in density space (left); Time evolution of the maximum BLK-MOC in density space**  
423 **between 22.45 and 23.85  $\text{kg m}^{-3}$  (right).**

424 Next, we identify the maximum MOC in density space for the Black Sea between 22.45 and 23.85  $\text{kg m}^{-3}$ , corresponding to  
425 depths of approximately 25 to 80 m (Ilicak et al., 2022). The MOC declined from 0.1 Sv in 1993 to a minimum of nearly 0.01  
426 Sv in 2010. After 2010, the MOC exhibited alternating periods of increase and decrease, but with an overall upward trend,

427 reaching its highest values of almost 0.12 Sv in 2022. Stanev et al. (2019) reported that the Black Sea MOC has weakened  
428 over the past 30 years, possibly due to anthropogenic global warming. In recent years, the CIL has nearly disappeared, as  
429 shown by observational data and reanalysis results (Stanev et al., 2019; Lima et al., 2021; Capet et al., 2020), as also discussed  
430 in the OHC section (Figures 9 and 10). Ilicak et al. (2022) associated the decline in MOC with the loss of CIL cold content  
431 between 1993 and 2010. However, since 2010, the MOC has started to increase, while the CIL is only present in 2012 and  
432 remains very weak in 2017 and 2022. Different water mass transformations could be the potential mechanisms behind an  
433 increase in the MOC. Specifically, an increase in salinity could compensate for the decrease in the formation of cold, dense  
434 water, which would otherwise weaken the circulation. Reanalysis model results show that there is an upward trend of SSS in  
435 the Black Sea. In addition, running multiple cycles of decadal reanalysis simulations is likely necessary to achieve a more  
436 accurate spin-up of the deep ocean. However, to investigate the detailed dynamics of the meridional overturning circulation  
437 (MOC) in the Black Sea, further research is required. This should involve using multi-cycle reanalysis model simulations  
438 combined with passive tracers, such as ideal age, to better understand the circulation patterns and timescales.

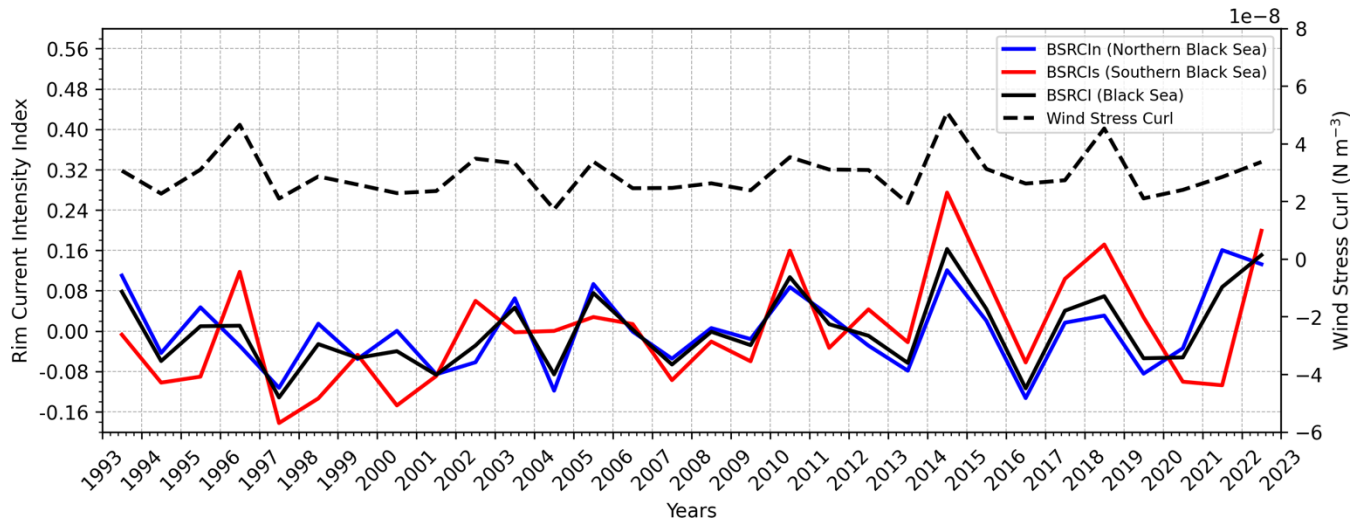
### 439 **3.2.3 The Rim Current interannual variability**

440 The Rim Current is the dominant cyclonic gyre that defines the general circulation of the Black Sea. The Black Sea Rim  
441 Current Intensity Index (BSRCI) measures the strength of this current in a given year relative to the multi-year average. It is  
442 based on the average surface current velocity in the Rim area confined by the isobaths of 200 and 1800 m. Two sections are  
443 chosen as representative for the Rim current: a northern section between 33°E–39°E, and a southern section between 31.5°E–  
444 35°E. For each section, the BSRCI is defined as:

$$445 \text{BSRCI} = \frac{\bar{v}_{ann} - \bar{v}_{cl}}{\bar{v}_{cl}} \quad (5)$$

446 with  $\bar{v}_{ann}$  the annual average surface current speed in the respective area and  $\bar{v}_{cl}$  the long-term average over the period 1993–  
447 2022. In this way, the index is close to zero when the annual mean state is near normal, while positive values indicate a stronger  
448 Rim Current, and negative values represent a weaker one (Peneva et al., 2021; von Schuckmann et al., 2021). The BSRCI OMI  
449 provides the intensity of the Rim Current in both the Northern and Southern Black Sea. In this study, we present updated  
450 results based on the latest data from the Black Sea reanalysis. The values are predominantly negative before 2010, with a  
451 notable negative peak below -0.2 in 1997 (Figure 12). After 2010, the values alternate between negative and positive, with  
452 positive peaks observed in 2014, 2017, 2020, and 2022. The BSRCI peak in 2014 exceeds 0.15 and reaches a maximum of  
453 over 0.25 in the southern branch. The intensity in both branches generally coincides, though the southern branch typically  
454 exhibits higher values. Peneva et al. (2021) also identified a peak in 2014 using results from the previous Black Sea reanalysis.  
455 The current analysis reveals a trend of +2.9% per decade, which is a value compatible with Peneva et al. (2021) as well.  
456 We also present the wind stress curl (Figure 12), diagnosed using the NEMO bulk formulation at the model’s native resolution,  
457 based on ERA5 wind data. As previously suggested by Stanev et al. (2000) and further examined by Peneva et al. (2021), the  
458 wind stress curl plays a key role in modulating the Rim Current. Our results support this relationship, showing strong agreement

459 between years of enhanced mean wind stress curl and increased intensity of the Black Sea Rim Current Index (BSRCI),  
 460 particularly in 2014 and 2018. This correspondence is especially evident in the southern section of the basin.



461  
 462 **Figure 12: Time series of the Black Sea Rim Current Index (BSRCI; black) at the north section (BSRCIn; blue), south section**  
 463 **(BSRCIs; red), the average (BSRCI) and its tendency for the period 1993-2020. The black dashed curve represents the annual mean**  
 464 **wind stress curl ( $\text{N m}^{-3}$ ) averaged for the Black Sea based on the ERA5 reanalysis.**

465 **4 Discussion and Outlook**

466 The new BLK-REA features a higher model resolution, providing a more consistent and accurate representation of Black Sea  
 467 physics. The updated configurations include the use of LOBCs, allowing improved water exchange through the Bosphorus  
 468 Strait. This enabled further refinements in the freshwater balance to be implemented, such as incorporating hourly precipitation  
 469 data and monthly runoff for the Danube River. These improvements were not possible in the previous Black Sea reanalysis,  
 470 as its closed boundaries required a controlled freshwater balance to prevent drifts in SSH.

471 Overall, the BLK-REA results are highly satisfactory for key ocean variables, including T, S, SLA. T accuracy exhibits strong  
 472 seasonality, with the basin-averaged RMSD of SST reaching its lowest value in spring ( $0.43\text{ }^{\circ}\text{C}$ ) and its highest in fall ( $0.61$   
 473  $^{\circ}\text{C}$ ). At depths within the seasonal thermocline, BLK-REA shows high RMSD errors for T in fall and summer, while errors  
 474 are lower in winter and spring. In contrast, salinity shows less seasonal variation, with the highest errors consistently occurring  
 475 in the 50–200 m layer throughout most of the period (Figure 3). Occasionally, salinity errors are also elevated at the surface.  
 476 SLA errors do not exhibit clear seasonality and have remained around  $0.02\text{ m}$  since 2000; an acceptable level considering that  
 477 the SLA observation error used in data assimilation is approximately  $0.04\text{ m}$ . Across all seasons, the highest SLA errors are  
 478 observed along the Rim Current, primarily due to high mesoscale activity along its pathway.

479 The reanalysis has proven to be an important tool for investigating the warming trend in the Black Sea, highlighting the recent  
 480 disappearance of the CIL. Both T and OHC exhibit a warming signal. In the 0–100 m layer, the warming trend is occasionally  
 481 interrupted, with decreases in OHC coinciding with periods of CIL presence, as observed in 2012, 2017 and 2022 (Figure 10).

482 Between 1993 and 2010, the decline in CIL formation may have influenced the MOC in the Black Sea. However, further  
483 investigations are needed to understand the recent increase in MOC and its relation with the CIL formation. Our results also  
484 reveal the significant influence of wind stress curl on the interannual variability of the Rim Current, with a particularly strong  
485 signal observed in its southern branch.

486 The BLK-REA dataset presented in this manuscript has been available online in the Copernicus Marine Service catalog since  
487 December 2024 and is extended monthly in Interim mode, which applies less refined configurations for preliminary processing.  
488 The Interim results are replaced annually with an extension of the reanalysis produced using optimal configurations and the  
489 assimilation of reprocessed data, which is considered the highest quality of observations. In alignment with the Black Sea near-  
490 real-time analysis and forecasting system, preparations for the next BLK-REA are already underway. Planned improvements  
491 include the integration of the Azov Sea in the model domain and the inclusion of runoff data from the European Flood  
492 Awareness System (Thielen et al., 2009). The plan also includes extending the reanalysis to cover previous decades, starting  
493 from 1980. This will allow for the extension of the existing OMIs and the preparation of new ones. In fact, tracking the warming  
494 signal in the Black Sea is essential, and our plan is to expand the analysis of the impacts of this warming, including monitoring  
495 marine heatwaves.

496 However, a major challenge is the limited availability of observations from 1980 onward. To address this gap, it may be  
497 necessary to integrate additional in-situ datasets beyond those available from SeaDataNet and Copernicus. Therefore,  
498 continuous monitoring of the Black Sea – particularly by enhancing observation systems – is crucial for maintaining the quality  
499 of reanalysis. In recent years, ongoing advancements in observation technologies and data integration have become  
500 increasingly important to further improve reanalysis accuracy and support long-term environmental studies.

## 501 **5 Data Availability**

502 The BLK-REA dataset presented in this study can be found in online repositories. The names of the repository/repositories  
503 and accession number(s) can be found below: <https://doi.org/10.48670/mds-00356>.

## 504 **6 Author contribution**

505 LL led the study, built the reanalysis system, and was involved in all parts of the work. DA and MI contributed to the  
506 development of the hydrodynamical model. They also shared useful ideas that improved the study in many ways. EJ helped  
507 set up the data assimilation strategies and also gave important suggestions to improve the work. FC helped with the validation  
508 of the reanalysis results. AS gave helpful comments that guided the research. PM supported the preparation of the in-situ  
509 observation data for the data assimilation and helped with the validation step. EC also gave useful suggestions that helped  
510 improve the work. All authors contributed to writing the article and approved the final version.

511 **7 Competing interests**

512 The authors declare that they have no conflict of interest.

513 **8 Acknowledgements**

514 The authors thank Y. Kim and one anonymous referee for their constructive comments that improved the manuscript.

515 **9 Financial support**

516 This research was funded by the Copernicus Marine Service for the Black Sea Monitoring and Forecasting Centre (Contract  
517 No. 21002L4-COP-MFC-BS-5400).

518 **References**

519 Altıok, H., and Kayışoğlu, M.: Seasonal and interannual variability of water exchange in the Strait of Istanbul, *Mediterr. Mar.*  
520 *Sci.*, 16(3), 644–655, 2015.

521 Beşiktepe, Ş. T., Sur, H. I., Özsoy, E., Latif, M. A., Oğuz, T., and Ünlüata, Ü.: The circulation and hydrography of the Marmara  
522 Sea, *Prog. Oceanogr.*, 34(4), 285–334, 1994.

523 Capet, A., Vandenbulcke, L., and Grégoire, M.: A new intermittent regime of convective ventilation threatens the Black Sea  
524 oxygenation status, *Biogeosciences*, 17, 6507–6525, <https://doi.org/10.5194/bg-17-6507-2020>, 2020.

525 Castellari, S., Pinardi, N., and Leaman, K.: A model study of air-sea interactions in the Mediterranean Sea, *J. Mar. Syst.*, 18,  
526 89–114, [https://doi.org/10.1016/s0924-7963\(98\)90007-0](https://doi.org/10.1016/s0924-7963(98)90007-0), 1998.

527 Chanut, J.: Nesting code for NEMO, Tech. rep., European Union: Marine Environment and Security for the European Area  
528 (MERSEA) Integrated Project, MERSEA-WP09-MERCA-TASK-9.1.1, 2005.

529 Ciliberti, S. A., Grégoire, M., Staneva, J., Palazov, A., Coppini, G., Lecci, R., Peneva, E., Matreata, M., Marinova, V., Masina,  
530 S., Pinardi, N., Jansen, E., Lima, L., Aydoğdu, A., Creti', S., Stefanizzi, L., Azevedo, D., Causio, S., Vandenbulcke, L., ...  
531 Agostini, P.: Monitoring and Forecasting the Ocean State and Biogeochemical Processes in the Black Sea: Recent  
532 Developments in the Copernicus Marine Service, *J. Mar. Sci. Eng.*, 9(10), 1146, <https://doi.org/10.3390/jmse9101146>, 2021.

- 533 Ciliberti, S. A., Jansen, E., Coppini, G., Peneva, E., Azevedo, D., Causio, S., Stefanizzi, L., Creti', S., Lecci, R., Lima, L.,  
534 Ilicak, M., Pinardi, N., and Palazov, A.: The Black Sea Physics Analysis and Forecasting System within the Framework of the  
535 Copernicus Marine Service, *J. Mar. Sci. Eng.*, 10(1), 48, <https://doi.org/10.3390/jmse10010048>, 2022.
- 536 Çokacar, T.: Cold Intermediate Water Formation in the Black Sea Triggered by March 2022 Cold Intrusions, *J. Mar. Sci. Eng.*,  
537 12(11), 2027, <https://doi.org/10.3390/jmse12112027>, 2024.
- 538 Courtier, P.: Variational methods, *J. Meteor. Soc. Japan*, 75, 211–218, 1997.
- 539 Dobricic, S., and Pinardi, N.: An oceanographic three-dimensional variational data assimilation scheme, *Ocean Model.*, 22,  
540 89–105, <https://doi.org/10.1016/j.ocemod.2008.01.004>, 2008.
- 541 Farina, R., Dobricic, S., Storto, A., Masina, S., and Cuomo, S.: A revised scheme to compute horizontal covariances in an  
542 oceanographic 3D-VAR assimilation system, *J. Comput. Phys.*, 284, 631–647, <https://doi.org/10.1016/j.jcp.2015.01.003>,  
543 2015.
- 544 Faugère, Y., Taburet, G., Ballarotta, M., Pujol, I., Legeais, J. F., Maillard, G., Durand, C., Dagneau, Q., Lievin, M., Sanchez  
545 Roman, A., and Dibarboure, G.: DUACS DT2021: 28 years of reprocessed sea level altimetry products, EGU General  
546 Assembly 2022, Vienna, Austria, 23–27 May 2022, EGU22-7479, <https://doi.org/10.5194/egusphere-egu22-7479>, 2022.
- 547 Garcia, H. E., Boyer, T. P., Baranova, O. K., Locarnini, R. A., Mishonov, A. V., Grodsky, A., Paver, C. R., Weathers, K. W.,  
548 Smolyar, I. V., Reagan, J. R., Seidov, D., and Zweng, M. M.: World Ocean Atlas 2018: Product Documentation, A. Mishonov,  
549 Technical Editor, 2019.
- 550 Good, S., Fiedler, E., Mao, C., Martin, M. J., Maycock, A., Reid, R., Roberts-Jones, J., Searle, T., Waters, J., While, J., and  
551 Worsfold, M.: The Current Configuration of the OSTIA System for Operational Production of Foundation Sea Surface  
552 Temperature and Ice Concentration Analyses, *Remote Sens.*, 12, 720, <https://doi.org/10.3390/rs12040720>, 2020.
- 553 Gunduz, G., Causio, S., Bonino, G., Vandenbulcke, L., Grégoire, M., Lima, L., Ciliberti, S., Ilicak, M., Aydogdu, A., Masina,  
554 S., Coppini, G., and Pinardi, N.: Coastal upwelling along the Turkish coast of the Black Sea: Its role in the distribution of the  
555 hydrographic properties, *J. Oper. Oceanogr.*, 15:sup1, s205–s211, <https://doi.org/10.1080/1755876X.2022.2095169>, 2022.
- 556 Haines, K.: Ocean reanalyses, in: *New Frontiers in Operational Oceanography*, edited by: Chassignet, E., Pascual, A., Tintoré,  
557 J., and Verron, J., Liguria: GODAE OceanView, 545–562, <https://doi.org/10.17125/gov2018.ch19>, 2018.

558 Ilicak, M., Federico, I., Barletta, I., Mutlu, S., Karan, H., Ciliberti, S. A., et al.: Modeling of the Turkish Strait system using a  
559 high resolution unstructured grid ocean circulation model, *J. Mar. Sci. Eng.*, 9, 769, <https://doi.org/10.3390/jmse9070769>,  
560 2021.

561 Ilicak, M., Causio, S., Ciliberti, S., Coppini, G., Lima, L., Aydogdu, A., Azevedo, D., Lecci, R., Cetin, D. U., Masina, S.,  
562 Peneva, E., Gunduz, M., and Pinardi, N.: The Black Sea overturning circulation and its indicator of change, *J. Oper. Oceanogr.*,  
563 15:sup1, s64–s71, <https://doi.org/10.1080/1755876X.2022.2095169>, 2022.

564 Ivanov, L. I., Backhaus, J. O., Özsoy, E., and Wehde, H.: Convection in the Black Sea during cold winters, *J. Mar. Syst.*, 31,  
565 65–76, [https://doi.org/10.1016/S0924-7963\(01\)00047-1](https://doi.org/10.1016/S0924-7963(01)00047-1), 2001.

566 Ingleby, B., and Huddleston, M.: Quality control of ocean temperature and salinity profiles—Historical and real-time data, *J.*  
567 *Mar. Syst.*, 65, 158–175, <https://doi.org/10.1016/j.jmarsys.2005.11.019>, 2007.

568 Korotaev, G., Oguz, T., Nikiforov, A., and Koblinsky, C.: Seasonal, interannual, and mesoscale variability of the Black Sea  
569 upper layer circulation derived from altimeter data, *J. Geophys. Res. Oceans*, 108, 3122, 2003.

570 Korotaev, G. K., Knysh, V. V., and Kubryakov, A. I.: Study of formation process of cold intermediate layer based on reanalysis  
571 of Black Sea hydrophysical fields for 1971–1993, *Izv. Atmos. Ocean. Phys.*, 50, 35–48,  
572 <https://doi.org/10.1134/S0001433813060108>, 2014.

573 Kubryakov, A. A., and Stanichny, S. V.: Mesoscale eddies in the Black Sea from satellite altimetry data, *Oceanology*, 55, 56–  
574 67, <https://doi.org/10.1134/S0001437015010105>, 2015.

575 Lima, L., Peneva, E., Ciliberti, S., Masina, S., Lemieux, B., Storto, A., et al.: Copernicus marine service ocean state report,  
576 issue 4, *J. Oper. Oceanogr.*, 13:sup1, s41–s47, <https://doi.org/10.1080/1755876X.2020.1785097>, 2020.

577 Lima, L., Ciliberti, S. A., Aydoğdu, A., Masina, S., Escudier, R., Cipollone, A., Azevedo, D., Causio, S., Peneva, E., Lecci,  
578 R., Clementi, E., Jansen, E., Ilicak, M., Cretì, S., Stefanizzi, L., Palermo, F., and Coppini, G.: Climate Signals in the Black Sea  
579 From a Multidecadal Eddy-Resolving Reanalysis, *Front. Mar. Sci.*, 8, 710973, <https://doi.org/10.3389/fmars.2021.710973>,  
580 2021.

581 Ludwig, W., Dumont, E., Meybeck, M., and Heussner, S.: River discharges of water and nutrients to the Mediterranean and  
582 Black Sea: major drivers for ecosystem changes during past and future decades?, *Prog. Oceanogr.*, 80, 199–217,  
583 <https://doi.org/10.1016/j.pocean.2009.02.001>, 2009.

584 Madec, G., and the NEMO team: NEMO ocean engine, *Sci. Notes Clim. Model. Cent.*, 27,  
585 <https://doi.org/10.5281/zenodo.1464816>, 2019.

586 Miladinova, S., Stips, A., Garcia-Gorriz, E., and Macias Moy, D.: Formation and changes of the Black Sea cold intermediate  
587 layer, *Prog. Oceanogr.*, 167, 11–23, <https://doi.org/10.1016/j.pocean.2018.07.002>, 2018.

588 Mulet, S., Buongiorno Nardelli, B., Good, S., Pisano, A., Greiner, E., Monier, M., et al.: Ocean temperature and salinity, in:  
589 Copernicus Marine Service Ocean State Report, *J. Oper. Oceanogr.*, 11:suppl.1, s13–s16,  
590 <https://doi.org/10.1080/1755876X.2018.1489208>, 2018.

591 Micaletto, G., Barletta, I., Mocavero, S., Federico, I., Epicoco, I., Verri, G., Coppini, G., Schiano, P., Aloisio, G., and Pinardi,  
592 N.: Parallel implementation of the SHYFEM (System of HydroDYNAMIC Finite Element Modules) model, *Geosci. Model Dev.*,  
593 15, 6025–6046, <https://doi.org/10.5194/gmd-15-6025-2022>, 2022.

594 Myroshnychenko, V., and Simoncelli, S.: SeaDataCloud Temperature and Salinity Historical Data Collection for the Black  
595 Sea (Version 1), *Ref. Prod. Info. Doc.*, SeaDataCloud, <https://doi.org/10.13155/56683>, 2018.

596 Myroshnychenko, V.: SeaDataCloud Temperature and Salinity Historical Data Collection for the Black Sea (Version 2), *Ref.*  
597 *Prod. Info. Doc.*, SeaDataCloud, <https://doi.org/10.13155/77211>, 2020.

598 Oguz, T., Latun, V. S., Latif, M. A., Vladimirov, V. V., Sur, H. I., Makarov, A. A., Özsoy, E., Kotovshchikov, B. B., Eremeev,  
599 V., and Unluata, U.: Circulation in the surface and intermediate layers of the Black Sea, *Deep Sea Res. Part I*, 40, 1597–1612,  
600 1993.

601 Oke, P. R., and Sakov, P.: Representation error of oceanic observations for data assimilation, *J. Atmos. Oceanic Technol.*, 25,  
602 1004–1017, <https://doi.org/10.1175/2007jtecho558.1>, 2008.

603 Özsoy, E., and Ünlüata, Ü.: Oceanography of the Black Sea: a review of some recent results, *Earth Sci. Rev.*, 42, 231–272,  
604 [https://doi.org/10.1016/s0012-8252\(97\)81859-4](https://doi.org/10.1016/s0012-8252(97)81859-4), 1997.

605 Peneva, E., Stanev, E., Ciliberti, S., Lima, L., Aydogdu, A., Marinova, V., and Valcheva, N.: Interannual variations of the  
606 Black Sea Rim Current, *J. Oper. Oceanogr.*, 14:sup1, s53–s59, <https://doi.org/10.1080/1755876X.2021.1946240>, 2021.

607 Pettenuzzo, D., Large, W. G., and Pinardi, N.: On the correction of ERA-40 surface flux products consistent with the  
608 Mediterranean heat and water budgets and the connection between basin surface total heat flux and NAO, *J. Geophys. Res.*,  
609 115, C06022, <https://doi.org/10.1029/2009JC005631>, 2010.

- 610 Podymov, O. I., Ocherednik, V. V., Silvestrova, K. P., and Zatsepin, A. G.: Upwellings and Downwellings Caused by  
611 Mesoscale Water Dynamics in the Coastal Zone of Northeastern Black Sea, *J. Mar. Sci. Eng.*, 11, 1628,  
612 <https://doi.org/10.3390/jmse11081628>, 2023.
- 613 Stanev, E. V., Le Traon, P.-Y., and Peneva, E. L.: Sea level variations and their dependency on meteorological and hydrological  
614 forcing: analysis of altimeter and surface data for the Black Sea, *J. Geophys. Res.*, 105(C7), 17203–17216,  
615 <https://doi.org/10.1029/1999JC900318>, 2000.
- 616 Stanev, E. V., Peneva, E., and Chtirkova, B.: Climate change and regional ocean water mass disappearance: case of the Black  
617 Sea, *J. Geophys. Res. Oceans*, 124, 4803–4819, <https://doi.org/10.1029/2019JC015076>, 2019.
- 618 Storto, A., Dobricic, S., Masina, S., and Di Pietro, P.: Assimilating along-track altimetric observations through local  
619 hydrostatic adjustment in a global ocean variational assimilation system, *Mon. Weather Rev.*, 139, 738–754,  
620 <https://doi.org/10.1175/2010mwr3350.1>, 2011.
- 621 Szekely, T., Gourrion, J., Pouliquen, S., and Reverdin, G.: CORA, Coriolis Ocean Dataset for Reanalysis, SEANOE,  
622 <https://doi.org/10.17882/46219>, 2024.
- 623 Thielen, J., Bartholmes, J., Ramos, M. H., and De Roo, A.: The European flood alert system—part 1: concept and development,  
624 *Hydrol. Earth Syst. Sci.*, 13(2), 125–140, 2009.
- 625 Yang, C., and Coauthors: Gathering Users and Developers to Shape Together the Next-Generation Ocean Reanalyses, *Bull.*  
626 *Amer. Meteor. Soc.*, 106, E419–E429, <https://doi.org/10.1175/BAMS-D-24-0034.1>, 2025.

627  
628